

Nanoscale architecture and dynamics of $\text{Ca}_v1.3$ channel clusters in cardiac myocytes revealed by single channel nanoscopy

Niko Schwenzer^{1,2,5}, Roman Tsukanov³, Tobias Kohl^{1,2,6}, Samrat Basak³, Fitzwilliam Seibert^{4,5,6,7}, Niels Voigt^{4,5,6}, Jörg Enderlein^{3,5}, Stephan E. Lehnart^{1,2,5,6,*}

¹ Department of Cardiology and Pneumology, University Medical Center Göttingen, Robert-Koch-Str. 40, 37075 Göttingen, Germany

² Cellular Biophysics and Translational Cardiology Section, Heart Research Center Göttingen, University Medical Center Göttingen, Robert-Koch-Str. 42a, 37075 Göttingen, Germany

³ Third Institute of Physics – Biophysics, University of Göttingen, Friedrich-Hund-Platz 1, 37077 Göttingen, Germany

⁴ Institute of Pharmacology and Toxicology, University Medical Center Göttingen, Robert-Koch-Straße 40, 37075 Göttingen, Germany

⁵ Cluster of Excellence “Multiscale Bioimaging: from Molecular Machines to Networks of Excitable Cells” (MBExC2067), University of Göttingen, 37073 Göttingen, Germany

⁶ DZHK (German Centre for Cardiovascular Research), partner site Göttingen, Robert-Koch-Str. 40, 37075 Göttingen, Germany

⁷ Nanion Technologies GmbH, Munich, Germany

* Corresponding author: slehnart@med.uni-goettingen.de

Abstract

The clustering of L-type calcium channels in cardiac myocytes presents an important mechanism for functional regulation of calcium signaling. Here we applied targeted super-resolution imaging techniques for the study of atrial-specific $\text{Ca}_v1.3$ channel clusters in human iPSC-derived atrial cardiomyocytes (hiPSC-aCM). We thereby clarified cluster localization, dimensions, architecture, and dynamics, which were largely unexplored previously. Live-cell STimulated Emission Depletion (STED) imaging identified that cell surface-localized clusters contained 9 channel molecules within 120 nm diameter on average. DNA Points Accumulation for Imaging in Nanoscale Topography (DNA-PAINT) optimized for molecular mapping revealed an irregular arrangement of channels with significant spacing. Single Particle Tracking (SPT) further evidenced that clustered channels do not associate into rigidly packed structures (oligomers or lattices), but rather co-diffuse in confined and stationary membrane nanodomains. Immunofluorescence showed consistent cell-surface colocalization with Ryanodine Receptor type 2 and Junctophilin-2 forming stable calcium release units, similar to dyadic junctions containing $\text{Ca}_v1.2$ in ventricular cardiomyocytes. Lastly, novel genetic constructs for live-cell imaging showed that the cytosolic C-terminal tail of $\text{Ca}_v1.3$ by itself is sufficient for cluster formation. In conclusion, a novel strategy for LTCC clustering studies in atrial cells was established, suitable for a wide range of super-resolution imaging techniques. Based on live-cell STED, DNA-PAINT and SPT data, we propose that $\text{Ca}_v1.3$ channel clusters consist of mobile individual channels inside defined membrane nanodomains.

35 Introduction

36 L-type calcium channels (LTCC) are essential for maintenance and regulation of heart contractility. In
37 cardiac myocytes, LTCC opening is triggered by action potential depolarization and leads to rapid,
38 transmembrane calcium influx and subsequent myofilament activation. As one of two cardiac LTCC,
39 $Ca_v1.3$ drives both pacemaking and contractility (Zaveri et al., 2023), supported by its selective ex-
40 pression in atrial cells and activation at more negative potentials compared to $Ca_v1.2$ (Z. Zhang et al.,
41 2005). LTCC form subdiffraction-sized clusters, which facilitate calcium release, cooperative gating and
42 protein interactions (Dixon et al., 2022). Previous studies on $Ca_v1.3$ clustering in neurons showed that
43 alternative splicing affects $Ca_v1.3$ function and cluster formation possibly through C-terminal protein
44 interactions with Calmodulin (CaM; Moreno et al., 2016), PDZ-binding proteins (Jenkins et al., 2010;
45 Stanika et al., 2016; Yang et al., 2023) and Junctophilin isoforms (Sahu et al., 2019). These findings
46 point towards analogous modulatory mechanisms governing $Ca_v1.3$ channel function in cardiomyo-
47 cytes.

48 Recent studies revealed new regulatory mechanisms of the cardiac channel homolog $Ca_v1.2$ (Del Vil-
49 lar et al., 2021; Liu et al., 2020) and it has become clear that the ‘classic’ model of functional upregu-
50 lation by direct channel phosphorylation is incorrect: β -adrenergic upregulation of $Ca_v1.2$ currents is
51 mediated by the small GTPase Rad, even when all potential phosphorylation sites on the α - and β -
52 channel subunits have been removed (Papa et al., 2022). An alternative and possibly converging
53 model of LTCC regulation involves the modulation of cooperativity via channel clustering (Baudel et
54 al., 2022; Del Villar et al., 2021), but the mechanisms and molecular dynamics of channel clustering
55 are not well understood. Earlier studies by the Santana group showed dimer-like bridging of channel
56 C-termini mediated by Calmodulin (Dixon et al., 2015; Moreno et al., 2016) and proposed a stochastic
57 self-assembly model of cluster formation (Sato et al., 2019), however there is no direct experimental
58 evidence for oligomerization-like cluster assemblies. Recently, increased clustering upon phosphoryla-
59 tion of the C-terminal $Ca_v1.2$ residue S1928 by PKA in vascular cells was reported (Baudel et al.,
60 2022). Clustering of the $Ca_v1.3$ isoform in cardiomyocytes was so far not characterized, as the channel
61 is not expressed in ventricular cells and presents the challenge of combining adequate cell isolation,
62 protein labeling and super resolution microscopy.

63 In this study, we show that human induced pluripotent stem cell-derived atrial cardiomyocytes
64 (hiPSC-aCM) expressing tagged $Ca_v1.3$ channels present a valuable experimental approach for unrav-
65 eling LTCC clustering mechanisms. We introduce a HaloTag- $Ca_v1.3$ fusion protein for live-cell STimu-
66 lated Emission Depletion (STED) imaging and Single Particle Tracking (SPT). Further, we use a corre-
67 sponding GFP fusion protein to perform DNA Points Accumulation for Imaging in Nanoscale Topogra-
68 phy (DNA-PAINT) at molecular-scale resolution (Schnitzbauer et al., 2017), which was not previously
69 reached in LTCC imaging studies. Combining the results of these super-resolution imaging techniques,
70 we address the molecular spatial arrangement of clustered channels within membrane nanodomains,
71 which was previously unclarified for LTCC in contrast to other ion channels. These findings serve as an
72 important foundation for future studies aiming to correlate cluster structure and its modulation with
73 functional readouts.

74

75 Results

76 Halo-tagged $\text{Ca}_v1.3$ channels form clusters in the plasma membrane of atrial cardiomyocytes

77 Human induced pluripotent stem cell-derived atrial cardiomyocytes (hiPSC-aCM) were used as a
78 model for the cellular physiology of atrial heart muscle (Cyganek et al., 2018). To investigate the clus-
79 tering of $\text{Ca}_v1.3$ calcium channels, an expression construct encoding the pore-forming subunit α_{1D} of
80 human $\text{Ca}_v1.3$ fused to an N-terminal HaloTag (Halo- $\text{Ca}_v1.3$) was expressed in hiPSC-aCM using transi-
81 ent transfection (Figure 1A, upper left). While the N-terminal tagging position was previously re-
82 ported as functionally inert (Grabner et al., 1998; Liu et al., 2020; H. Zhang et al., 2005), we confirmed
83 a physiological voltage-current response for our construct by patch clamp measurement (Figure S1).

84 For live-cell imaging of hiPSC-aCM expressing Halo- $\text{Ca}_v1.3$, the cells were labeled with a cell-permea-
85 ble HaloTag ligand (HTL) conjugated to a fluorogenic JF646 fluorophore. Subsequent confocal imaging
86 revealed spot-like signals (Fig. 1A, magenta) representing $\text{Ca}_v1.3$ channel clusters. The signals local-
87 ized predominantly to the plasma membrane, which was confirmed by co-staining with fluorescently
88 labeled Cholesterol (green). Spot-like $\text{Ca}_v1.3$ signals were only observed in transfected cells and not in
89 apparently untransfected neighboring cells, highlighting the specificity of our labeling approach. The
90 focal plane was then shifted to the coverslip-adherent plasma membrane of cardiomyocytes, result-
91 ing in the highest density of spot-like Halo- $\text{Ca}_v1.3$ signals. To accurately resolve individual clusters be-
92 low the diffraction limit, super-resolution STED imaging was applied (Fig. 1B). Compared to confocal
93 imaging, more distinct and smaller signal shapes were detected by STED, presumably representing
94 individual clusters. Interestingly, cluster signals often appeared in grouped arrangements, which cor-
95 responded to unresolved, single spots in the confocal image.

96 To quantify the abundance and size of cluster signals, image analysis was applied to a larger dataset
97 of equivalently recorded STED images (Fig. 1C). Due to the high variability of signal spot intensities,
98 thresholding-based methods were insufficient for segmentation and a custom approach based on ro-
99 bust peak finding and expansion was implemented (see Methods section). This segmentation method
100 led to reliable cluster detection even for low-intensity or directly adjacent signals, resulting in a spa-
101 tial density of 2.0 ± 0.5 (mean \pm s.d.) clusters/ μm^2 . Exemplary segmentation outlines are presented
102 on raw image data in Fig. 1C. Across the dataset, these outlines encompassed cluster areas of $0.013 \pm$
103 $0.008 \mu\text{m}^2$ corresponding to equivalent diameters of 122 ± 35 nm when assuming circular shapes. The
104 histogram of measured areas shows a right-skewed frequency distribution, demonstrating that cluster
105 diameters were typically around 100 nm and rarely exceeded 200 nm.

106 Using the same image data, molecular counting of dye molecules was applied to segmented clusters
107 by referencing their brightness against calibration samples with defined dye numbers (Fig. S2). Halo-
108 Tag labeling is well-suited for this approach, since precisely one dye molecule is covalently bound to
109 each labeled channel. Hence the approximate number of $\text{Ca}_v1.3$ channels within each cluster signal
110 can be extracted with low statistical variance, despite not considering that a fraction of channels is
111 unlabeled. The mean background signal surrounding each cluster signal was subtracted from the con-
112 tained signal intensity. As a result, we found 9 ± 12 channels per cluster in a right-skewed distribution
113 (median = 5, Fig. 1D). By relating the channel count of each cluster to its area, we were able to calcu-
114 late intra-cluster channel densities, which amounted to 612 channels/ μm^2 . Notably this result greatly
115 differs from a theoretical limit of $\sim 10,000$ channels/ μm^2 expected for oligomer-like dense channel
116 packing, which was not nearly reached in our measurement (99th percentile: 1625 channels/ μm^2).

117 DNA-PAINT resolves channel arrangements and confirms loosely packed cluster structure

118 The molecular architecture of LTCC clusters has not been resolved thus far. Ground State Depletion
119 (GSD) and Stochastic Optical Reconstruction Microscopy (STORM) were previously used for super-res-
120 olution cluster imaging but did not reach true molecular-scale resolution. Moreover, antibody-based

121 labeling has been a hindering factor, due to the large physical displacement (so-called linkage error)
122 between label and epitope. We aimed to surpass these limitations by combining direct Cav1.3 chan-
123 nel tagging with DNA-PAINT, a technique that reaches molecular-scale resolution through the use of
124 exchangeable fluorophores – the main limiting factor in single-molecule fluorescence microscopy
125 (Schnitzbauer et al., 2017).

126 Analogous to our Halo-Cav1.3 construct, we expressed GFP-Cav1.3 in hiPSC-aCM and labeled for DNA-
127 PAINT in fixed cells using the commonly used GFP nanobody (Fig. 2A; Ries et al., 2012; Sograte-Idrissi
128 et al., 2019). Imaging was performed using a custom-built Total Internal Reflection Fluorescence
129 (TIRF) setup with single-molecule sensitivity to image Cav1.3 channels selectively in the coverslip-ad-
130 herent plasma membrane. Single molecule binding events of Atto 643 (or Atto 550)-labeled imager to
131 its complementary docking strand were highly specific and sparsely distributed (Fig. 2B). The emitter
132 positions were localized over time series of 30,000 to 50,000 frames to build a super-resolution image
133 reconstruction. The resulting DNA-PAINT images showed clustered signal distributions, which were in
134 full agreement with GFP fluorescent signals recorded at diffraction-limited resolution, confirming the
135 specificity of DNA-PAINT binding events. A magnified image region shown in Fig. 2C demonstrates
136 that clusters of GFP-Cav1.3 were super-resolved by DNA-PAINT, leading to groups of puncta corre-
137 sponding to each diffraction-limited GFP-fluorescence spot. Individual cluster magnifications (Fig. 2D)
138 revealed a disordered arrangement of clearly separable puncta. Since puncta appearance was mostly
139 uniform and non-overlapping, countable puncta were assumed to reflect single channel positions.

140 We benchmarked our reconstruction quality by Nearest Neighbor Analysis (NeNa; Endesfelder et al.,
141 2014) as the basis for further optimization. For initial reconstructions, a localization precision $\sigma = 12.5$
142 ± 1 nm was measured (Fig. 2E), which was improved to 9.8 ± 1.2 nm after applying drift and vibration
143 correction based on a recently published algorithm (Cnossen et al., 2021). Moreover, localization
144 merging (as described by Martens et al., 2021) and filtering (see Methods section) led to a drastic im-
145 provement of localization precision to 4.1 ± 0.3 nm, which was deemed sufficiently small to resolve
146 individual Cav1.3 channels with a channel diameter of 10 nm and hence similar expected minimal
147 spacing (Yao et al., 2022). Along with these optimization steps, we observed a successive improve-
148 ment of resolution in the reconstructions without a noticeable loss of spot detection sensitivity (Fig.
149 S3A).

150 To characterize clustering quantitatively, molecular mapping was performed by identification of signal
151 maxima in DNA-PAINT reconstructions, presumably indicating single channel positions (Fig. 2F). Nota-
152 bly, adjacent maxima with a distance of 12 nm were reliably resolved (white arrows in Fig. 2F). Chan-
153 nel positions were then subjected to DBSCAN clustering (Ester et al., 1996; Siddig et al., 2020). The
154 optimal parameter value $\epsilon = 100$ nm was chosen and used to detect the highest number of clusters
155 ($2.5 \pm 0.5 \mu\text{m}^{-2}$), whereas increased ϵ values led to merging of adjacent clusters and increased vari-
156 ance (Fig. S3B,C). We note that the detected cluster density is close to the value of $2.0 \mu\text{m}^{-2}$ obtained
157 by STED-based cluster analysis in living cells. Using the obtained molecular maps, we computed me-
158 dian nearest-neighbor distances (NND) of 47 nm and 32 nm when considering all or only clustered
159 channels, respectively. The frequency distribution of NND for all channels (Fig. 2G) showed a local
160 plateau at 100 nm, thus reaffirming the chosen ϵ value. Notably, only 19% of clustered channels were
161 in close mutual proximity defined by NND values below 20 nm. Lastly, we quantified DBSCAN-based
162 cluster detections, which were defined by areas of $0.013 \pm 0.020 \mu\text{m}^2$ (Fig. 2H) containing 7 ± 7 chan-
163 nel spots (Fig. 2I), with both distributions showing an exponential falloff. Taken together, these results
164 cross-validate our STED-based cluster analysis (see Table 1) and support a model of a widely spaced,
165 disordered distribution of clustered Cav1.3 channels.

166 **Ca_v1.3 channels are laterally mobile despite static cluster positions**

167 To explore the dynamics of individual Ca_v1.3 channels within clusters, a dual labeling approach was
168 introduced for living hiPSC-aCM expressing Halo-Ca_v1.3: First, sparse labeling of single channels was
169 attained by application of HTL-JF646 at minimal concentration (see Methods section). Directly after, a
170 concurrent ensemble labeling of clusters was achieved by applying HTL-JF549 at saturating concentra-
171 tion. The resulting signal distributions were evaluated by live-cell, single-molecule TIRF imaging of the
172 basal plasma membrane (Fig. 3A, left), leading to whole-cluster labeling in the JF549 channel, and al-
173 ternatively well-separated single-molecule signals in the JF646 channel. For either channel, untrans-
174 fected control cells showed almost no signals in comparison (Fig. 3A, center).

175 To evaluate single channel and cluster mobilities by single particle tracking, movies of each red
176 (JF646) and green (JF549) channel fluorescence were recorded consecutively for each cell. The result-
177 ing particle tracks for an exemplary cell are shown as a temporal overlay (Fig. 3A, right). Notably,
178 tracks of both labeling modes were restricted to small domains, but JF646-labeled single channel
179 tracks occupied larger areas compared to JF549-labeled cluster tracks. In the latter case, signals origi-
180 nated from multiple labeled channels within subdiffraction-sized domains; therefore, an averaged,
181 central cluster position was detected and tracked. As indicated by nearly point-like track overlays, all
182 recorded cluster positions were strongly confined or immobile.

183 The mobility of individual channels and clusters was then quantified by track-based diffusion analysis
184 (Fig. 3B). For each track, we evaluated the mean jump distance (MJD) over the 30 ms frame interval
185 and applied mean squared displacement (MSD) analysis to retrieve the diffusion coefficient. MJD of
186 84 ± 43 nm were measured for single channels, showing a broad distribution of values ranging from
187 20 to 210 nm (98% of data). In contrast, cluster positions showed MJD of only 50 ± 19 nm, which dis-
188 tributed rather symmetrically ranging from 10 to 100 nm (98% of data). This indicates that individual
189 channels diffused more rapidly and showed more heterogeneous movement compared to cluster po-
190 sitions. Notably, mathematical modeling of immobile positions considering localization uncertainty
191 (see Methods section) resulted in MJD of 44 ± 12 nm, which indicates by comparison that cluster po-
192 sitions showed little to no mobility. Next, we examined channel and cluster diffusion by MSD analysis.
193 The fit of individual MSD curves along the first five lag times generated short-term diffusion coeffi-
194 cients (D), which are a more robust measure of diffusivity that accounts for localization error (Micha-
195 let, 2010). For both single channels and cluster positions, the frequency distributions of D were ap-
196 proximately lognormal (Fig. 3B, right). Median D values were more than threefold higher for single
197 channels ($D = 0.0054 \mu\text{m}^2/\text{s}$) as compared to cluster positions ($D = 0.0015 \mu\text{m}^2/\text{s}$), confirming a signifi-
198 cant mobility of single channels. For reference, a threshold value of $0.001 \mu\text{m}^2/\text{s}$ (Di Biase et al., 2011;
199 Folci et al., 2018; Hansen et al., 2018) is commonly used to define immobile spots, which classified
200 46% of clusters but only 20% of single channels as immobile based on short-term diffusion. Inde-
201 pendently, confocal time lapse data confirmed immobility of cluster positions at lower temporal but
202 higher spatial resolution for time scales of up to 10 minutes (Fig. S4).

203 **Nanodomain traversal of Ca_v1.3 channels corresponds to dynamic channel clustering**

204 Importantly, we validated our assumption of single-molecule labeling: We almost exclusively ob-
205 served single-step bleaching in intensity traces of long tracks (Fig. S5A) and found the distribution of
206 mean track intensity to be monomodal (Fig. S5B, top-left) reflecting that multi-labeled channels were
207 only rarely measured and thus did not interfere with the interpretation of diffusion coefficients. We
208 also assured that both imaging modes obtained similar spot brightness and track lengths to ensure an
209 unbiased comparison (Fig. S5B top versus bottom).

210 When looking into the shape of long single channel tracks (Fig. 3C), we found two predominant mo-
211 tion types: First, we mostly identified mobile channels, which appeared highly confined to one or

212 multiple membrane domains and showed variable diffusion speed. Second, with lesser abundance,
213 we identified immobile channels, showing much smaller and consistent displacements around a de-
214 fined position. For the first motion type, multi-domain diffusion was observed for particularly long
215 tracks, with a clearly higher channel mobility across inter-domain spaces (examples shown in Fig. 3D).
216 The observed switching of motion types across consistent nanodomains seems to reflect the occa-
217 sional transit of channels from one cluster to another. Notably, the high diffusivity state generally
218 lasted less than one second before returning to the confined state for longer time periods.

219 To quantify the confinement of single channels in terms of domain size, we noted that power-law fit-
220 ting of MSD is unsuitable for rather short track lengths and low diffusivity compared to the localiza-
221 tion error (Kepten et al., 2015). Instead, we determined the convex hull area and radius of gyration
222 for each track (Fig. 3E), which are direct geometrical measurements and thus do not rely on curve fit-
223 ting (Golan & Sherman, 2017; Luković et al., 2013). We limited our analysis to a time window length
224 of 300 ms (10 frames), which ensured consistency across variable track lengths (Fig. S4B). We thereby
225 measured convex hull areas of $0.015 \pm 0.026 \mu\text{m}^2$ and radii of gyration of $63 \pm 36 \text{ nm}$ for single chan-
226 nel tracks, which is consistent with previously determined cluster dimensions obtained by STED and
227 DNA-PAINT (Table 1). In contrast, JF549-labeled cluster positions showed vastly smaller convex hull
228 areas of $0.004 \pm 0.003 \mu\text{m}^2$ and radii of gyration of $39 \pm 16 \text{ nm}$, which primarily reflect the localization
229 error around immobile positions (see Methods section).

230 **Ca_v1.3 clusters robustly assemble as Ca²⁺ release units with RyR2 and Junctophilin-2**

231 Next, we examined the organization of calcium release units (CRU) in hiPSC-aCM. CRUs are special-
232 ized membrane sites characteristic for primary cardiomyocytes, where sarcoplasmic reticulum-con-
233 tained Ryanodine Receptor type 2 (RyR2) and sarcolemmal LTCC are juxtaposed as functional units,
234 which are scaffolded by Junctophilin-2 (JPH2; Brandenburg et al., 2019; Weninger et al., 2022; Z. F.
235 Yang et al., 2022) and mediate Ca²⁺-induced Ca²⁺ release from the sarcoplasmic reticulum. While
236 CRUs in adult atrial cardiomyocytes of highly developed species are found both at the cell surface and
237 in intracellular tubular membrane networks (Brandenburg et al., 2018), immature cardiomyocytes in-
238 cluding hiPSC-aCM do not feature these membrane networks and thus inherently rely on cell-surface
239 localized domains for calcium release. This suits well to quantitative imaging of the coverslip attached
240 membrane in a consistent, reproducible focal plane (compare Fig. 1).

241 Accordingly, three-channel confocal immunofluorescence of hiPSC-aCM labeled for Halo-Ca_v1.3, JPH2
242 and RyR2 showed spot-like signals for each target protein at the cell surface (Fig. 4A). All three pro-
243 teins colocalized to a large degree, which resulted in white spot coloring in the overlay image. Colo-
244 calization was confirmed in the basal imaging plane (Fig. 4B), which rendered the lateral distribution
245 of each protein across the cell surface and revealed a high number of three-channel-colocalized
246 spots. The pattern of spatial correlation was exemplified by intensity line profiles (Fig. 4C), showing
247 that indeed most signal peaks constituted all three proteins. To quantify the recruitment of Ca_v1.3 to
248 calcium release units (CRUs), three-channel image segmentation (Fig. 4D) and colocalization analysis
249 (Fig. 4E) were applied to a dataset of similarly recorded cell-surface images: We first analyzed the
250 fraction of colocalized Ca_v1.3 signal and thus found that 65% of Ca_v1.3 signal mass was RyR2-colocal-
251 ized, 61% was JPH2-colocalized, and 51% was double-colocalized, indicating an efficient channel re-
252 cruitment to CRUs. The results were reproduced by inversion of secondary antibodies and imaging
253 channels for RyR2 and JPH2 in the same experiment (Fig. 4E). Lastly, we analyzed Ca_v1.3-colocaliza-
254 tion from the perspective of CRU composition, defining CRU signal as the product of JPH2 and RyR2
255 signal. Thereby we found that $86\% \pm 3\%$ of CRU signal mass colocalized with Ca_v1.3, indicating that
256 atrial CRUs very consistently harbor Ca_v1.3 channels.

257 We also determined the colocalization of Halo- and GFP-tagged Ca_v1.3 with several other subcellular
258 compartments and proteins (Fig. S6). Live-cell co-staining with fluorescently labeled Cholesterol as a

259 nanodomain marker showed an exclusion-like pattern rather than colocalization in the basal plasma
260 membrane, highlighting that $\text{Ca}_v1.3$ clusters are independent of cholesterol-containing lipid domains
261 (Fig. S6A). Immunodetection of endogenous Caveolin-3 (Cav3), a marker of caveolar nanodomains,
262 showed only mild colocalization with $\text{Ca}_v1.3$ (Fig. S6B). Labeling of the endoplasmic reticulum showed
263 no colocalization (Fig. S6C), indicating that GFP- $\text{Ca}_v1.3$ was efficiently expressed and transported to
264 the plasma membrane. No colocalization between Halo- $\text{Ca}_v1.3$ and either sarcomeric alpha-actinin or
265 Junctophilin-1 was observed (Fig. S6D,E). To test whether the association of $\text{Ca}_v1.3$ and JPH2 requires
266 other cardiac proteins, both proteins were expressed in HEK293 cells and found to strongly colocalize
267 in the basal plasma membrane, pointing towards a tissue-independent, intrinsic association of both
268 proteins.

269 **The C-terminal cytosolic tail of $\text{Ca}_v1.3$ is sufficient for cluster formation**

270 Alternative splicing of human $\text{Ca}_v1.3$ primarily truncates the C-terminal protein sequence, leading to
271 a shortening of the cytosolic C-terminal tail (CTT) from 694 to 180 amino acids in the short (42A) iso-
272 form. Since the CTT contains several important protein interaction sites (e.g. for CaM, JPH2, AKAP)
273 and its splicing was shown to modulate channel clustering (Moreno et al., 2016; Stanika et al., 2016),
274 we hypothesized that the CTT may be involved in, necessary, or even sufficient to confer clustering of
275 $\text{Ca}_v1.3$ channels. We conceived an accessible experimental approach to address this by generating
276 novel fusion proteins concatenating extracellular N-terminal HaloTag (Svendsen et al., 2008) with in-
277 tracellular CTT sequence of either $\text{Ca}_v1.3$ isoform. We then expressed these constructs in hiPSC-aCM
278 and applied surface-selective labeling using HTL-Alexa488 for live-cell confocal imaging to observe the
279 extent of cluster formation.

280 For both constructs and a control construct lacking CTT sequence, signals were predominantly found
281 at the cell surface, as confirmed by co-staining of the plasma membrane (Fig. 5). Interestingly, basal
282 plane imaging showed a segregation of signals into cluster-like shapes for both CTT constructs (Fig.
283 5A, magenta), but an increased abundance of clustered signals for the long versus short CTT isoform
284 (Fig. 5B). As expected, the control construct lacking $\text{Ca}_v1.3$ sequence showed a highly homogenous
285 membrane signal (Fig. 5C), indicating that there is no intrinsic ability of the extracellular HaloTag to
286 form clusters. The clustering of these constructs was quantified by image analysis, which confirmed a
287 significantly higher cluster abundance for the long versus short CTT construct (mean 17.4% versus
288 7.9%, $p < 0.0001$, Fig. 5D). Notably, the surface expression level (Fig. 5E) and relative cluster bright-
289 ness indicative of cluster size (Fig. 5F) were not significantly different, reflecting that CTT truncation
290 mainly affected cluster abundance but not other parameters. The control construct of transmem-
291 brane-anchored HaloTag without CTT notably showed a much higher expression level, but a near-ab-
292 sence of clustering.

293 Since the observed clustering of CTT constructs may depend on pre-existing endogenous Ca_v channel
294 clusters in hiPSC-aCM, we similarly investigated CTT cluster formation in transfected HEK293 CT6232
295 cells (expressing only the accessory channel subunits β_3 and $\alpha_2\delta_1$, but not α_{1D}). In these cells lacking
296 cardiac proteins, we again observed robust cluster formation of both CTT constructs as compared to
297 the control construct (Fig. S7). Similar to hiPSC-aCM, a higher cluster abundance for the long versus
298 short CTT isoform was observed. These results confirmed that $\text{Ca}_v1.3$ CTT is sufficient to form $\text{Ca}_v1.3$
299 clusters even in the absence of cardiac-specific accessory proteins and pre-existing clusters.

300 Discussion

301 Herein nanoscale imaging of human $\text{Ca}_v1.3$ channel clusters was pioneered in the hiPSC-aCM expres-
302 sion system with labeling strategies novel to L-type calcium channels. Consequently, we provide the
303 first model of $\text{Ca}_v1.3$ cluster assembly in cardiomyocytes, which can be readily compared to existing
304 data in neuronal model systems. The use of hiPSC-aCM provided a physiological cellular framework
305 for the assembly of functional calcium channels, resembling spontaneously contracting cardiomyo-
306 cytes in an early developmental stage (Emanuelli et al., 2022; Pourrier & Fedida, 2020). The atrial sub-
307 type-directed differentiation implicates an endogenous expression of LTCC in these cells (Chapotte-
308 Baldacci et al., 2023; Cyganek et al., 2018). In contrast to primary cardiomyocytes, hiPSC-CM are ame-
309 nable to gene transfection (Yuan et al., 2022), which was harnessed in our study to transiently trans-
310 fect with tagged $\text{Ca}_v1.3$ variants. Since we selectively labeled these tagged $\text{Ca}_v1.3$ variants and not
311 endogenous $\text{Ca}_v1.3$ in our imaging experiments, simultaneous occurrence of both types of channels
312 within clusters cannot be completely excluded. Offsetting this, we can assume that relative protein
313 cell surface abundance was clearly weighted towards tagged $\text{Ca}_v1.3$ due to a titration effect: in con-
314 trast to endogenous channels, tagged $\text{Ca}_v1.3$ was overexpressed, while LTCC surface trafficking and
315 residency depends on molecular assembly with β -subunits, limited by the available endogenous pool
316 (Conrad et al., 2021; Stanika et al., 2016). In addition, ER-resident tagged $\text{Ca}_v1.3$ channels and aggre-
317 gates were hardly observed in transfected cells, owing to a lower protein biosynthesis rate compared
318 to heterologous expression systems and the sensitive unfolded protein response for ion channels in
319 hiPSC-CM (Liu et al., 2018). Consequently, potential overexpression artifacts on cluster analysis are
320 considered non-significant.

321 Cluster analysis was performed on the canonical, full-length human $\text{Ca}_v1.3_{42}$ sequence, the most
322 abundant isoform in human cardiomyocytes (Singh et al., 2008). The pore-forming subunit α_{1D} was
323 tagged at the N-terminus preserving channel voltage-gating, while the C-terminus is crucial for regu-
324 latory functions that may be perturbed by fusion-tagging. In addition, we considered that alternative
325 tagging of the accessory β -subunit (Conrad et al., 2021; Del Villar et al., 2021; Liu et al., 2020) was un-
326 suitable for our study since $\text{Ca}_v\beta$ can bind other Ca^{2+} channel isoforms and performs intracellular
327 functions (Vergnol et al., 2022). We developed independent and synergistic cluster analysis workflows
328 on hiPSC-aCM expressing tagged $\text{Ca}_v1.3$ proteins. Live-cell quantitative STED and DNA-PAINT imaging
329 determined cluster size and geometry data, while live-cell SPT produced the first mobility data on
330 $\text{Ca}_v1.3$ channels in cardiomyocytes. Both STED and DNA-PAINT detected cell surface channel clusters
331 of on average ~ 120 nm diameter containing 7–9 channel molecules. Notably live-cell STED excluded
332 potential fixation artifacts previously reported (Huebinger et al., 2018; Sgrate-Idrissi et al., 2020) and
333 introduced channel counting based on brightness referencing (Schmied et al., 2012). Brightness cali-
334 bration assumed a similar labeling efficiency and linear signal to dye number relation for calibration
335 beads and within cluster nanodomains in situ. The method offers a higher counting range and live-cell
336 compatibility in contrast to widely used photobleaching analysis (Hummert et al., 2021). Importantly,
337 spatial fluorophore densities observed in this study vastly argue against quenching effects known for
338 directly adjacent fluorophores (Schröder et al., 2019).

339 While STED-based size metrics were limited by a spatial resolution of ~ 70 nm, our DNA-PAINT imag-
340 ing approach using GFP-targeted $\text{Ca}_v1.3$ (Fig. 2) attained molecular-scale resolution down to 4 nm lo-
341 calization precision, which was not achieved by any previous study of LTCC clustering, e.g. compared
342 to 16 nm in GSD imaging (Moreno et al., 2016). We note that additional, variable displacement errors
343 caused by the undetermined mobility of the cytosolic $\text{Ca}_v1.3$ N-terminus and the physical size of the
344 nanobody (~ 4 nm) used for detection possibly reduced the effective resolution. However, these ef-
345 fects were deemed insignificant compared to previous approaches using indirect immunodetection
346 (Sgrate-Idrissi et al., 2019). The developed procedures for DNA-PAINT and subsequent data analysis

347 thus are sufficient to resolve adjacent channels of 10 nm diameter (Yao et al., 2022) and resulted in
348 similar cluster metrics as live-cell STED imaging, confirming the validity of our approach (Table 1).

349 DNA-PAINT revealed a rather large, non-uniform spacing of clustered channels (median NND = 32 nm)
350 and a low incidence of directly adjacent channels (19% of channels with NND < 20 nm). These obser-
351 vations argue against both oligomerization-like isotropic packing of channels and constitutive dimeri-
352 zation. Interestingly, we did not observe any grid-like arrangements, which are characteristic for skele-
353 tal muscle Cav1.1 and RyR1 clusters (Schredelseker et al., 2005). In this regard, we found that Cav1.3
354 channel arrangement rather corresponds to the stochastic nature of cardiac RyR2 channel clusters
355 (Asghari et al., 2014; Jayasinghe et al., 2018). Interestingly, a previous study in primary hippocampal
356 neurons measured similar Cav1.3 channel counts per cluster by bleach step counting and the same
357 exponential distribution of cluster areas (Moreno et al., 2016), although we measured approximately
358 threefold larger cluster areas on average in cardiomyocytes. Tissue-dependent characteristics were
359 previously not evidenced between neurons and cardiomyocytes, but rather for cochlear inner hair
360 cells, which contain multifold larger Cav1.3 clusters (Neef et al., 2018). Differences in cluster size
361 could rather arise from different segmentation strategies, especially since comparison of the pre-
362 sented images indicates similar dimensions of DNA-PAINT and GSD-imaged clusters.

363 Additional data for our Cav1.3 clustering model was gathered by SPT analysis of channel mobility (Fig.
364 3), that included both sparse single-channel labeling and ensemble labeling for tracking whole clus-
365 ters. HaloTag-based covalent labeling enabled the use of bright and photostable organic fluoro-
366 phores, achieving robust motion tracking by state-of-the-art algorithms (Kuhn et al., 2021). The re-
367 sulting trajectories were suitable for track-based diffusion analysis and readily comparable between
368 both imaging modes, owing to matched spot intensities and tracking durations (Fig. S5). A direct com-
369 parison revealed that individual channels exhibited much higher diffusivity than independently
370 tracked cluster positions (median D 0.0059 versus 0.0015 $\mu\text{m}^2/\text{s}$), thus excluding the possibility of rig-
371 idly packed cluster structures. Notably, the absence of multi-step bleaching events in our SPT data in-
372 dicates that the majority of tracks correspond to single fluorophores, and thus single channels. Given
373 that we identified confined mobility as the major motion type across all single channel SPT tracks, we
374 interpreted the occupied nanodomains as being equivalent to clusters. These cluster domains were
375 described by an average gyration radius across all single channel tracks of 64 nm, which fits to cluster
376 diameters of around 120 nm reported by STED imaging and DNA-PAINT. Thus, our multi-faceted
377 methodological approach is devoid of major technical compromises and shows consistent independ-
378 ent readouts and output parameters, building up a new model of Cav1.3 cluster configurations. Our
379 SPT approach measured channel mobilities that were also in line with previously reported values of
380 neuronal Cav1.2 channels (D = 0.005 $\mu\text{m}^2/\text{s}$; Di Biase et al., 2011). Similar to the cited study, we evi-
381 denced the traversal of channels across multiple confined domains, which implies that clusters might
382 dynamically recruit and disband individual channels within relatively short dwell times on the order
383 of seconds. The possibility for partial disassembly of clusters stands in contrast to previous mathe-
384 matical modeling of LTCC clustering (Sato et al., 2019), however a stochastic assembly process may
385 hold true.

386 Interestingly, Cav1.3 cluster positions in hiPSC-aCM were nearly immobile over long time scales. This
387 is likely due to scaffolding at defined membrane locations, given the highly organized nature of cardi-
388 omyocytes including multi-protein CRUs with membrane tethering proteins like Junctophilin-2. In this
389 line we confirmed that Cav1.3, RyR2 and JPH2 consistently associate at the cell surface (Fig. 4), form-
390 ing stable calcium release units, equivalent to peripheral dyadic junctions containing Cav1.2 in ven-
391 tricular cardiomyocytes (Franzini-Armstrong et al., 1999). A direct interaction site between LTCC and
392 JPH2 was recently postulated (Gross et al., 2021; Z. F. Yang et al., 2022), which is supported by our
393 data showing strong colocalization of Cav1.3 and JPH2 not only in hiPSC-aCM but also upon co-ex-
394 pression in HEK293 cells lacking cardiotypical proteins. In parallel these interactions could account for

395 the observed fraction of immobile $\text{Ca}_v1.3$ channels in SPT. However, our Cholesterol and Cav3 stain-
396 ings did not reproduce CRU association with lipid rafts (Poulet et al., 2021). Interestingly, previous
397 studies reported the association of potassium channels $\text{K}_v2.1$, $\text{K}_{\text{Ca}1.1}$ and $\text{K}_{\text{Ca}3.1}$ with neuronal CRUs,
398 which further promoted LTCC clustering and function through direct interactions (Sahu et al., 2019;
399 Vierra et al., 2019; Vivas et al., 2017). This demonstrates that CRUs are dynamic, heterogenous struc-
400 tures enabling multifold protein interactions, in line with the emerging clustering model for LTCC. As
401 indicated additionally by significant channel spacing and mobility, clustered $\text{Ca}_v1.3$ channels are pre-
402 sumably intermixed with relevant interactors in the same nanodomain. This organization enables effi-
403 cient channel regulation through transient, rather than constitutive interactions. Whether correla-
404 tions exist between spatial arrangements and dynamics for distinct CRU constituents remains specu-
405 lative but appears to be likely. Analogously these principles have been more extensively researched
406 for Ca_v2 channels in neuronal systems, however underlying a different functional context (Heine et
407 al., 2020; Perni & Beam, 2021). Notably, the confinement of presynaptic Ca_v2 channels to cluster do-
408 mains was shown to be dependent on alternative C-terminal splicing (Heck et al., 2019; Held et al.,
409 2020) and similar organizational mechanisms were found for K_v channel clustering (Lewin et al., 2020;
410 Sadegh et al., 2017).

411 For $\text{Ca}_v1.3$ channels, there are two broadly expressed splice variants: Full-length, canonical $\text{Ca}_v1.3_{42}$
412 and C-terminally truncated $\text{Ca}_v1.3_{42A}$, which have distinct electrophysiological properties and a tissue-
413 specific relative abundance, implying a cell-context specific fine-tuning of channel activation
414 (Kuzmenkina et al., 2019). Interestingly, endogenous cytosolic peptides of $\text{Ca}_v1.3$ distal C-termini
415 (DCT) competitively bind to $\text{Ca}_v1.3$ channels and downregulate their function (Y. Yang et al., 2022). To
416 assess the relevance of $\text{Ca}_v1.3$ C-termini for cluster formation, we took advantage of our flexible
417 hiPSC-aCM expression system and introduced novel, artificial constructs of membrane-anchored
418 $\text{Ca}_v1.3$ C-terminal tail (CTT) for live-cell imaging. Cluster analysis surprisingly revealed that $\text{Ca}_v1.3$ CTT
419 intrinsically formed cell-surface clusters. Moreover, cluster abundance was clearly reduced for the
420 shorter CTT sequence (180 aa of $\text{Ca}_v1.3_{42A}$) as opposed to the canonical CTT sequence (694 aa of
421 $\text{Ca}_v1.3_{42}$) (Fig. 5). This clearly demonstrates that while the proximal, structured C-terminus is suffi-
422 cient for cluster formation, there are additional protein interactions on the extended CTT of $\text{Ca}_v1.3_{42}$
423 that appear to enhance cluster formation or maintenance in the plasma membrane. Given that we
424 observed a similar experimental outcome for ectopic expression in HEK293 cells (Fig. S7), it seems
425 that the required protein interactions underlying this effect are not specific to cardiac myocytes.

426 This leads us to a comparison of putative protein interactions on the proximal versus extended (full-
427 length) CTT to relate our overall findings to possible clustering mechanisms. The extended CTT of
428 $\text{Ca}_v1.3_{42}$ contains binding sites for JPH2, AKAP family and PDZ-binding proteins, which are relevant
429 scaffolds for LTCC and may spatially define cluster nanodomains or mediate channel tethering (Choi
430 et al., 2022; Sahu et al., 2019; Stanika et al., 2016; Yang et al., 2023). While these interactions may
431 enhance clustering, none of them appear to be strictly required for clustering, given that we showed
432 cluster formation for the short CTT sequence of $\text{Ca}_v1.3_{42A}$. This proximal, structured C-terminus only
433 contains the EF-Hand and IQ domains, which are important binding sites for modulation by CaM and
434 CaBP (Scharinger et al., 2015). CaM binding was previously reported to mediate C-terminal channel
435 coupling through dimer-like bridging (Moreno et al., 2016) and confirmed to be transient in nature
436 (Kuzmenkina et al., 2019). Whether this mechanism is sufficient for multifold channel associations
437 beyond dimerization was so far unknown but is supported by our data showing clustering of short
438 $\text{Ca}_v1.3$ CTT constructs. However, we observed a strongly ($\sim 50\%$) reduced clustering of the short ver-
439 sus long CTT construct. This indicates that a mechanism involving CaM may be sufficient to form clus-
440 ters, but not stabilize them, leading to disassembly or internalization. Interestingly, in tsA-201 cells
441 and primary neurons (Moreno et al., 2016; Stanika et al., 2016), the equivalent channel isoform
442 $\text{Ca}_v1.3_{42A}$ showed only a mild ($\sim 20\%$) reduction of cluster areas compared to full-length $\text{Ca}_v1.3_{42}$. The

443 small effect size compared to our study of corresponding CTT constructs indicates that additional,
444 CTT-independent mechanisms may increase the stability of Cav1.3 channel clusters. Further investiga-
445 tion of clustering mechanisms and their functional impact using super-resolution and live-cell imaging
446 studies presents a promising future direction for the research of LTCC regulation and pathophysiology.

447 In conclusion, we established a novel approach for researching LTCC clustering based on N-terminal
448 channel tagging in hiPSC-aCM tailored for innovative multiscale super-resolution microscopy. Based
449 on complementary results including DNA-PAINT, live-cell STED and SPT data, we propose that Cav1.3
450 channel clusters consist of relatively mobile individual channels with large interspacing in defined
451 membrane domains, which facilitate transient channel interactions with regulatory and scaffolding
452 proteins to effectively regulate calcium signaling.

453 **Materials and Methods**

454 **Plasmids**

455 Cav1.3 human cDNA (accession number NM_001128840.2, UniProt Q01668-1) was de-novo synthe-
456 sized including an N-terminal 'GGG' linker. This cDNA was assembled into a vector encoding N-termi-
457 nal fusion to the HaloTag (pHTN_HaloTag_CMV-neo, Promega G7721) using restriction cloning, yield-
458 ing the Halo-Cav1.3 plasmid. To alternatively generate an N-terminal mEGFP fusion, HaloTag was ex-
459 changed by restriction cloning to yield the GFP-Cav1.3 plasmid.

460 A sequence encoding N-terminal HaloTag fused to the transmembrane sequence of non-clustering
461 Integrin β_1 (NM_002211.4) was generated as described by Svendsen et al. (2008) and assembled into
462 an EFS-promotor driven vector (pRP-EFS, Vectorbuilder) to generate the control construct 'Hal-
463 oTM_Ctrl'. For Cav1.3 CTT constructs, the insert sequence was fused with cDNA encoding CTT se-
464 quence of either human Cav1.3₄₂ (NM_001128840.2) or Cav1.3_{42A} (XM_047448874.1), starting at
465 amino acid position D1468, generating the long and short CTT plasmids 'HaloTM_Cav13CT-L' and 'Hal-
466 oTM_Cav13CT-S'.

467 **Cell culture and transfection**

468 Human induced pluripotent stem cells (hiPSC) that were derived from healthy human donor cells
469 (isWT1.14, kindly provided by the UMG Stem Cell Unit) were cultured in StemFlex medium (Gibco
470 A3349401) and differentiated to atrial cardiomyocytes according to an established protocol
471 (Kleinsorge & Cyganek, 2020). Cardiomyocytes were purified in glucose-free selection medium after
472 differentiation and then cultured in RPMI 1640 medium (Gibco 72400021) with B-27 supplement
473 (Thermo Fisher 17504044) lacking antibiotics. All differentiations showed spontaneous contractility.
474 For imaging experiments, cells were seeded on Matrigel-coated glass-bottom imaging dishes (ibidi
475 81158) at subconfluent density. Two days after seeding, growth medium containing 2 μ M CHIR99021
476 (Merck 361559) and 10% fetal bovine serum (Gibco 16140071) were added to enhance transfection
477 efficiency (Yuan et al., 2022). Cells were transfected the following day using 0.6–1 μ g of plasmid and
478 Viafect reagent (Promega E4981, 6 μ l/ μ g plasmid). The medium was exchanged the following day to
479 regular culture medium. Cells were imaged at 4–7 days after transfection.

480 HEK293 cells with constitutive expression of Cav subunits β_3 and $\alpha_2\delta_1$ and inducible expression of α_{1D}
481 (Charles River Laboratories CT6232) were cultured in DMEM/F12 medium containing selection antibi-
482 otics and 0.6 μ M isradipine (Sigma I6658). For imaging experiments, cells were seeded on fibronectin-
483 coated glass-bottom imaging dishes (ibidi 81158) in a growth medium lacking selection antibiotics.
484 Transfection was performed using Lipofectamine 3000 reagent (Invitrogen L3000008) according to
485 the manufacturer's instructions with 0.6–1 μ g plasmid DNA per imaging dish. A washing step was per-
486 formed 3 h after transfection using a fresh culture medium. Microscopy experiments were carried out
487 1–2 days after transfection. For electrophysiology, the same protocol was applied to 6-well plates
488 with 2 μ g plasmid being added per well. The induction of α_{1D} subunit expression with Tetracycline was
489 generally not performed, unless indicated.

490 **Cell labeling for microscopy**

491 For Halo-Cav1.3 imaging by confocal and STED microscopy, a labeling solution containing 100 nM
492 JF646-HTL (Promega GA1121) in phenol red-free culture medium was freshly prepared. Live-cell la-
493 beling was performed by incubation of hiPSC-aCM in labeling solution for 30 min at 37°C, optionally
494 followed by co-labeling with Cholesterol-Star488/ -StarOrange (Abberior 0206, 40 nM) for 10 min or
495 ER-Tracker Red (Invitrogen E34250, 1 μ M) for 30 min in cell culture medium at 37°C. After labeling, a
496 wash-out step was performed by incubation with fresh culture medium for 2 h at 37°C. Afterwards,
497 cells were washed thrice and imaged in live-cell imaging solution (Thermo Fisher A14291DJ).

498 Dual channel labeling for SPT experiments was performed in phenol red-free culture medium: First, a
499 solution of 250 pM JF646-HTL was applied for 10 min at 37°C. Then, a solution containing 50 nM
500 JF549-HTL (Promega GA1110) was applied for 15 min at 37°C. This was followed by two washing steps
501 and incubation in culture medium for 2 h at 37°C to achieve effective wash-out of unbound ligands.
502 The cells were then washed four times with live-cell imaging solution for 5 min each and subse-
503 quently imaged.

504 For confocal imaging of CTT constructs, hiPSC-aCM or HEK293 cells were incubated with a labeling
505 solution containing both cell-impermeant HTL-Alexa488 (Promega G1001, 1 µM) and Cellmask Deep
506 Red Plasma Membrane stain (Invitrogen C10046, 5 µg/mL) in phenol-red free culture medium for 10
507 min at 37°C. Then, cells were washed twice with medium and twice with live-cell imaging solution be-
508 fore imaging. Cellmask stain was optionally exchanged for Cholesterol-PEG-KK114 (Brandenburg et
509 al., 2018), yielding similar membrane staining. Notably, alternative HaloTag labeling using Alexa660-
510 HTL (Promega G8471) at 3.5 µM concentration did not generate a sufficient labeling outcome.

511 For immunofluorescence of cells expressing Halo-Cav1.3, live-cell incubation with JF646-HTL was per-
512 formed as described above. Afterward, cells were washed twice with phosphate buffered saline (PBS)
513 and fixed for 10 min by 4% paraformaldehyde (PFA) diluted in Dulbecco's PBS containing Ca²⁺ and
514 Mg²⁺ (DPBS; Gibco 14040083), then blocked and permeabilized for 1 h in blocking buffer (10% bovine
515 calf serum and 0.1% Triton X-100 in DPBS). Cells were then incubated with primary antibody diluted
516 in blocking buffer overnight at 4°C. This was followed by a secondary antibody incubation in a block-
517 ing buffer for 90 min at room temperature. Cells were imaged in DPBS, SlowFade Diamond (Invitrogen
518 S36967) or ProLong Gold (Invitrogen P36930).

519 DNA-PAINT labeling of GFP-Cav1.3 transfected cells was carried out according to the immunofluores-
520 cence protocol, but cells were fixed in 4% PFA for 20 min at RT, both before and after the labeling pro-
521 cedure to achieve post-fixation. The blocking buffer was supplemented with 0.1 mg/mL sheared
522 salmon sperm DNA (Thermo Fisher 15632011) and 0.05% w/v dextran sulfate (Merck D4911) and Im-
523 age-iT FX reagent (Invitrogen I36933) was applied for 10 min after blocking to reduce nonspecific im-
524 ager binding (Koester et al., 2022; Youn et al., 2023). GFP nanobody conjugated to R4-docker DNA
525 (sequence 5' → 3': ACACACACACACACACA, Metabion) was applied in dilution buffer (3% BCS, 0.1%
526 Triton X-100, 0.05 mg/mL sheared salmon sperm DNA in DPBS) for 1 h at RT.

527 The following antibodies were used in this study:

Species	Target	Cat number	Dilution
Rabbit	RyR2	Sigma HPA 020028	1:500
Mouse	RyR2	Thermo Fisher mA3-916	1:500
Mouse	JPH2	SantaCruz sc377086	1:500
Rabbit	JPH2	Invitrogen 40-5300	1:100
Nanobody	GFP	NanoTag N0304	1:500
Mouse	Cav3	BD Biosciences 610421	1:500
Mouse	ACTN2	Sigma A7811	1:500
Rabbit	JPH1	Thermo Fisher 40-5100	1:200

528

529 **Microscopy setup and image acquisition**

530 Confocal and STED imaging were performed using an Abberior Expert Line inverted microscope
531 equipped with an oil immersion objective lens (Olympus UPlanSApo 100x NA 1.4), pulsed excitation

532 lasers at wavelengths 640/591/485 nm, pulsed STED laser at wavelength 775 nm, Abberior QUAD
533 scanner and avalanche photodiode detectors (Excelitas Technologies SPCM-AQRH). Acquisition set-
534 tings for quantitative JF646 STED imaging were as follows: 30% excitation laser power at 640 nm, 12%
535 STED laser power, pixel size 25 nm, pixel dwell time 64 μ s, time gating window 0.5–6 ns. Confocal im-
536 ages were generated at variable excitation powers depending on the experiment and a pixel size of 80
537 nm. Image channels were recorded separately in line steps to avoid fluorescence crosstalk. All imag-
538 ing was performed at RT.

539 DNA PAINT and SPT measurements were performed on a custom-built TIRF optical setup, as de-
540 scribed elsewhere (Sograte-Idrissi et al., 2019). The optical configuration is shown in Figure S8. Briefly,
541 488 nm (Omicron PhoxX+ 488-100), 561 nm (Changchun MGL-FN-561-100), and 638 nm (Omicron
542 PhoxX+ 638-150) lasers were used for sample excitation. A neutral density filter (Thorlabs NE10A-A)
543 in tandem with the variable neutral density filter ND (Thorlabs NDC-50C-4-A) were used to adjust the
544 laser excitation power. The laser beam was coupled into a single-mode optical fiber (SMF, Thorlabs
545 P1-460B-FC-2) with a typical coupling efficiency of 40%. After exiting the optical fiber, the collimated
546 laser beam was expanded by a factor of 3.6X using telescope lenses (TL1 and TL2). The typical excita-
547 tion intensity at the sample was ~ 1 kW/cm² for high-photon flux DNA-PAINT imaging.

548 The laser beam was focused onto the back focal plane of the TIRF objective (Olympus UAPON 100X
549 oil, 1.49 NA) using achromatic lens L1 (Thorlabs AC508-180-AB). Mechanical shifting of the beam with
550 respect to the optical axis was done through a translation stage (TS, Thorlabs LNR25/M) to allow for a
551 change between different illumination schemes: EPI, HILO, and TIRF. The smooth lateral positioning of
552 a sample was achieved by using a high-performance two-axis linear stage (Newport M-406). In addi-
553 tion, an independent one-dimensional translation stage (Thorlabs LNR25/M) together with a differen-
554 tial micrometer screw (Thorlabs DRV3) was used to shift the objective along the optical axis for focus-
555 ing on different sample planes. The spectral separation of the collected fluorescence light from the
556 reflected excitation light was achieved using a multi-band dichroic mirror (DM, Semrock Di03
557 R405/488/532/635), which directed the emitted fluorescence light towards the tube lens L2 (Thorlabs
558 AC254-200-A-ML). The field of view was physically limited in the emission path by an adjustable slit
559 aperture (OWIS SP60) positioned in the image plane. Lenses L3 (Thorlabs AC254-100-A) and L4
560 (Thorlabs AC508-150-A-ML) were used to re-image the emitted fluorescence light from the slit onto
561 an emCCD camera (Andor iXon Ultra 897). A band-pass filter (BPF, BrightLine HC 692/40) was used to
562 further block the scattered excitation light. The total magnification of the optical system on the
563 emCCD camera was 166.6X, resulting in an effective pixel size in the sample space of 103.5 nm.

564 DNA-PAINT acquisition was performed in a TIRF mode, with the exposure time of 30 ms and EM gain
565 of 500. First, cells with GFP expression level were selected and then DNA PAINT movies of 30–50k
566 frames were acquired. The imager concentration was in the range of 0.5–1 nM. Single particle track-
567 ing was performed in a TIRF mode with the exposure time of 30 ms and EM gain of 500 (JF646) or 100
568 (JF549). Typically, the acquisition of a single movie took 2–5 minutes. All experiments were done at
569 22°C temperature, which was crucial for the mechanical stability of the optical setup.

570 **Confocal and STED image analysis**

571 Image analysis was performed in ImageJ Fiji (Schindelin et al., 2012) version 1.54f. All analyses were
572 applied selectively to annotated cell areas. For STED image segmentation, the FFT bandpass filter
573 (2.5–20 px) was applied to remove high-frequency noise and unstructured background signal. Candi-
574 date signal spots were identified in the filtered image by maxima detection and peak expansion to
575 half-maximal intensity (FWHM) using the ImageJ plugin *Interactive H-Watershed*. Resulting candidate
576 regions of interest (ROI) were discarded if containing less than 5 pixels or a mean intensity less than
577 50% above the background signal. All remaining ROIs representing specific signals were used for area
578 and brightness measurements. Cluster diameters were calculated from segmented areas using $d =$

579 $2\sqrt{A/\pi}$ assuming circular shape. Signal brightness was measured in raw image data and corrected for
580 local background by subtraction of the mean brightness of a ring-like ROI obtained by differential en-
581 largement of each cluster ROI by 4 versus 2 pixels.

582 For molecular counting in STED images (Fig. S2), DNA Origami reference structures containing 23 ± 3
583 and 7 ± 1 JF646 dye binding sites were purchased from GATTAquant and immobilized on the surface
584 of ibidi glass-bottom imaging dishes coated with BSA-biotin. A calibration measurement was per-
585 formed by applying the same quantitative nanoscopy workflow as for Halo-Cav1.3 cluster samples.
586 The resulting distribution of single particle brightness was used to determine a single dye brightness
587 value for molecular counting of channel molecules in cluster ROIs.

588 For confocal-based colocalization analysis, three-channel images were binarized using FFT bandpass
589 filtering (4–40 px) followed by automated local thresholding ('Otsu', radius 20 px) in each channel.
590 Colocalization was determined in raw image data as the fraction of above-threshold Cav1.3 signal
591 mass in binarized JPH2-, or RyR2-positive area, or JPH2-RyR2 double-positive area (as defined by
592 Manders M1 colocalization coefficient). To analyze CRU composition, CRU signals were defined as the
593 pixel-wise product of JPH2 and RyR2 signals. Then, the fraction of above-threshold CRU signal mass
594 colocalized with binarized Cav1.3 signals was calculated (corresponding to Manders M2).

595 For confocal-based cluster analysis of CTT constructs, images were smoothed by a Gaussian filter ($\sigma =$
596 1 px) and then binarized using automated thresholding ('Moments'). Resulting spots were quantified
597 by 'Analyze Particles' with particle size 6–120 px². Larger particles were not analyzed as they were
598 atypical for clusters and may originate from endosomes.

599 The ImageJ macro code used in this section is provided as Supplementary Software.

600 **DNA-PAINT image reconstruction and analysis**

601 Raw DNA-PAINT image sequences were processed in ImageJ using the *ThunderSTORM* plugin (Ovesny
602 et al., 2014). The following parameters were used for emitter localization:

603 Lowered Gaussian filter with sigma = 1.6 px, peak intensity threshold = 1.5*std(Wave.F1),
604 weighted least squares fit, PSF = integrated Gaussian, initial sigma = 1.6 px, fitting radius = 3 px

605 For drift and vibration correction, the recently published DME algorithm (Cnossen et al., 2021, version
606 1.2.1) was implemented using MATLAB R2022A. We increased the robustness of long-term drift track-
607 ing by applying DME iteratively for decreasing time bins, which performed better compared to redun-
608 dant cross correlation (RCC), which was suggested in the original implementation. Our optimization
609 efforts resulted in the following parameters:

610 iterative: usercc = false, coarse_frames_per_bin = 5000/ 500/ 10, gradientstep = 5e-5/ 5e-5/
611 5e-6, crlb = 4 σ / 2 σ / σ

612 final step: framesperbin = 1, gradientstep = 1e-6, crlb = σ

613 The obtained improvements in localization precision were evaluated by NeNa, which was applied to
614 the central image region (code adapted from Martens et al., 2021). To further increase localization
615 precision, detections were merged in ThunderSTORM with parameters *max. dist. = 30 nm*, *max.*
616 *frames = 4*, *max. off frames = 0* and then filtered by the criteria *detections > 2 & uncertainty < 10 nm*.
617 Subsequently, a density filter with *radius = 12 nm*, *n_min = 4* was applied to discard spurious signals.
618 The reconstruction was then generated by Gaussian rendering with *sigma = 5 nm*, *magnification = 26*,
619 resulting in 4 nm image pixel size.

620 For molecular mapping and cluster analysis, a custom-written analysis was applied using MATLAB
621 R2022A. The analysis was limited to manually annotated cell footprints. Briefly, reconstructions were

622 smoothed by the H-maxima transform (*imhmax*) followed by local maxima detection (*imregion-*
623 *almax*), thus detecting putative channel positions by combining localizations and binding events origi-
624 nating from the same binding site. These positions were then subjected to DBSCAN clustering with
625 *minPts = 3* and $\epsilon = 100$ nm (see Fig. S3C). The points comprising each cluster were then outlined using
626 the *boundary* function. The resulting polygons were expanded by $d = 10$ nm using the *polybuffer* func-
627 tion to account for physical channel dimensions and localization error. Nearest-neighbor distances
628 across all points or only clustered points were determined using the *knnsearch* function.

629 The MATLAB code used in this section is provided as Supplementary Software.

630 **Single particle tracking and motion analysis**

631 Localization and tracking of single-molecule image series was performed using the *TrackIt* package
632 (Kuhn et al., 2021) running in MATLAB R2022A. The following parameters were used:

633 JF646: *u-track random motion, threshold factor = 1.25, tracking radius = 4 px, min track length*
634 *= 10, gap frames = 3*

635 JF549: *u-track random motion, threshold factor = 2, tracking radius = 2 px, min track length =*
636 *10, gap frames = 1*

637 Mean jump distance (MJD) and diffusion coefficient (D) were determined for each track using the
638 same software. D values were derived using a linear fit of the first 5 MSD values based on the equa-
639 tion $MSD(\tau) = 4 D \tau + b$ where MSD is the mean squared displacement over all localization pairs for
640 any given lag time τ (based on the frame interval), and b is an offset term reflecting the experimental
641 localization error (Michalet, 2010). For confocal time series in Fig. S4 containing relatively long tracks,
642 the logarithmic fit function $MSD(\tau) = 4 D \tau^\alpha + b$. was applied, where α is an exponent indicative of
643 the motion type (Lerner et al., 2020). For visualization, tracks were rendered with temporal time cod-
644 ing using the color map *turbo*.

645 Confinement metrics were calculated for each track containing at least 10 localizations by averaging
646 over a sliding time windows of 300 ms duration. Convex hull areas were calculated using the *convhull*
647 function. The radius of gyration (R_{Gyr}) was calculated as the root mean square of pointwise distances
648 to the center of mass. Notably, an apparent motion of immobile particles is always detected in experi-
649 mental SPT data due to localization errors. Mathematical modeling of this effect was used to estimate
650 the influence on our measurements. We determined an approximate localization precision (σ) of 25
651 nm in our SPT images using ThunderSTORM. Subsequently, the following formulae (Golan & Sherman,
652 2017) were used to determine MJD and R_{Gyr} values for immobile particles:

$$653 \text{MJD} = \sqrt{\pi} \sigma = 44.3 \text{ nm}$$

$$654 \text{R}_{Gyr} = \sqrt{2} \sigma = 35.4 \text{ nm}$$

655 To generate value distributions resembling our experiment as a point of comparison, we performed a
656 Monte-Carlo simulation ($n = 10,000$ runs) of immobile particles according to the experimental track
657 length distribution (Fig. S5B) and estimated localization precision $\sigma = 25 \pm 5$ nm, resulting in:

$$658 \text{MJD} = 44 \pm 11 \text{ nm}$$

$$659 \text{R}_{Gyr} = 34 \pm 8 \text{ nm}$$

660 The MATLAB code used in this section is provided as Supplementary Software.

661 **Patch clamp measurements**

662 HEK293 CT6232 cells were seeded on fibronectin-coated 6-well plates and transfected with 2 μg of
663 plasmid per well encoding Halo- or GFP-tagged $\text{Ca}_v1.3$ as described earlier. For control conditions,
664 $\text{Ca}_v1.3^{\text{WT}}$ (α_{1D}) was induced by adding 1 $\mu\text{g}/\text{mL}$ Tetracycline (Sigma T7508) to the culture medium in
665 parallel to transfections. Cells were harvested one day after transfection as follows: After washing with
666 pre-warmed PBS, cells were dissociated by incubation with 0.25% Trypsin-EDTA solution (Thermo
667 Fisher 25200056) for 30 s at 37°C. The cells were then suspended in growth medium and centrifuged
668 at 100 g, 4°C for 5 min. The cell pellet was then resuspended in divalent-free HBSS (Gibco) at 4 °C.
669 Automated patch-clamp experiments were conducted with the SyncroPatch 384 (Nanion Technologies
670 GmbH) device with thin borosilicate glass, single aperture 384-well chips (NPC384T 1 x S-type). Appli-
671 cation of negative pressure (150–250 mbar) allowed for whole-cell access. $\text{Ca}_v1.3$ currents were elicited
672 with a voltage-step protocol at 0.5 Hz with a holding potential of -80 mV followed by a 100 ms test-
673 pulse at -40 mV to +70 mV with 5 mV increments. Experiments were carried out at 22–24 °C. Internal
674 solution contained (in mmol/L): EGTA 10, HEPES 10, CsCl 10, NaCl 10, CsF 110, pH 7.2 (with CsOH). Bath
675 solution contained (in mmol/L): HEPES 10, NaCl 140, glucose 5, KCl 4, CaCl_2 2, MgCl_2 1, pH 7.4 (with
676 KOH). Currents were recorded with a Tecella amplifier controlled by PatchControl 384 software. Re-
677 cordings were analyzed offline with DataControl 384 software (both: Nanion Technologies GmbH)
678 (Seibert et al., 2022).

679 **General data analysis**

680 Data was visualized and statistically analyzed using GraphPad Prism version 10 and MATLAB R2022A.

681 **Data and materials availability statement**

682 The generated biological materials will be provided by the authors upon request. The generated code
683 for image data processing and analysis is provided as Supplementary Software.

684 **Acknowledgements**

685 We are grateful for the excellent technical assistance by Timo Schulte, Brigitte Korff and Elli Rehbein-
686 Bode.

687 Stephan E. Lehnart is a principal investigator of DZHK (German Centre for Cardiovascular Research).

688 **Funding**

689 Funded by the Deutsche Forschungsgemeinschaft (DFG) under Germany's Excellence Strategy–EXC
690 2067–390729940 to SEL, JE and NV.

691 This work was supported by the Deutsche Forschungsgemeinschaft to NV (VO 1568/3-1, VO 1568/4-
692 1, IRTG1816 project 12, SFB1002 project A13) and by the DZHK to NV (German Center for Cardiovas-
693 cular Research, 81X2300189 and 81X4300102, “DNAfix”).

694 JE and SB are grateful to the European Research Council (ERC) via project “smMIET” (Grant agree-
695 ment No. 884488) under the European Union's Horizon 2020 research and innovation program.

696 **Author contributions**

Conceptualization: NS, TK, JE, SEL

Methodology: NS, RT, TK, FS

Software: NS

Investigation: NS, RT, SB, FS

Formal analysis: NS, RT

Visualization: NS, SB

Writing – original draft: NS

Writing – review & editing: NS, TK, SEL

Supervision: TK, NV, JE, SEL

Funding acquisition: SEL, JE, NV

697 References

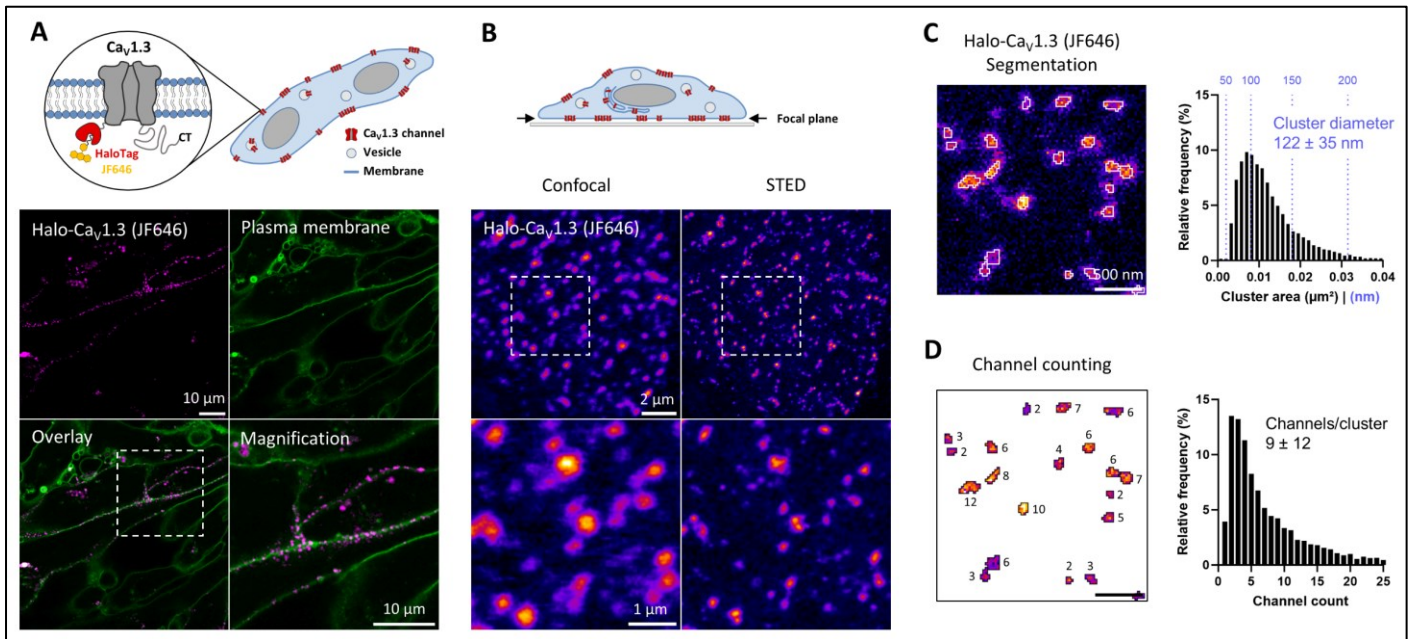
- 698 Asghari, P., Scriven, D. R., Sanatani, S., Gandhi, S. K., Campbell, A. I., & Moore, E. D. (2014). Nonuniform and variable
699 arrangements of ryanodine receptors within mammalian ventricular couplons. *Circ Res*, *115*(2), 252-262.
700 <https://doi.org/10.1161/CIRCRESAHA.115.303897>
- 701 Baudel, M. M. A., Flores-Tamez, V. A., Hong, J., Reddy, G. R., Maillard, P., Burns, A. E., Man, K. N. M., Sasse, K. C., Ward, S. M.,
702 Catterall, W. A., Bers, D. M., Hell, J. W., Nieves-Cintrón, M., & Navedo, M. F. (2022). Spatiotemporal Control of
703 Vascular Cav1.2 by alpha1C S1928 Phosphorylation. *Circ Res*, *131*(12), 1018-1033.
704 <https://doi.org/10.1161/CIRCRESAHA.122.321479>
- 705 Brandenburg, S., Pawlowitz, J., Eikenbusch, B., Peper, J., Kohl, T., Mitronova, G. Y., Sossalla, S., Hasenfuss, G., Wehrens, X. H.,
706 Kohl, P., Rog-Zielinska, E. A., & Lehnart, S. E. (2019). Junctophilin-2 expression rescues atrial dysfunction through
707 polyadic junctional membrane complex biogenesis. *JCI Insight*, *4*(12). <https://doi.org/10.1172/jci.insight.127116>
- 708 Brandenburg, S., Pawlowitz, J., Fakuade, F. E., Kownatzki-Danger, D., Kohl, T., Mitronova, G. Y., Scardigli, M., Neef, J., Schmidt,
709 C., Wiedmann, F., Pavone, F. S., Sacconi, L., Kutschka, I., Sossalla, S., Moser, T., Voigt, N., & Lehnart, S. E. (2018). Axial
710 Tubule Junctions Activate Atrial Ca²⁺ Release Across Species. *Frontiers in Physiology*, *9*, 1227.
711 <https://doi.org/10.3389/fphys.2018.01227>
- 712 Chapotte-Baldacci, C. A., Pierre, M., Djemai, M., Pouliot, V., & Chahine, M. (2023). Biophysical properties of Na_v1.5 channels
713 from atrial-like and ventricular-like cardiomyocytes derived from human induced pluripotent stem cells. *Sci Rep*,
714 *13*(1), 20685. <https://doi.org/10.1038/s41598-023-47310-6>
- 715 Choi, S., Vivas, O., Baudot, M., & Moreno, C. M. (2022). Aging Alters the Formation and Functionality of Signaling
716 Microdomains Between L-type Calcium Channels and beta2-Adrenergic Receptors in Cardiac Pacemaker Cells.
717 *Frontiers in Physiology*, *13*, 805909. <https://doi.org/10.3389/fphys.2022.805909>
- 718 Clossen, J., Cui, T. J., Joo, C., & Smith, C. (2021). Drift correction in localization microscopy using entropy minimization.
719 *Optics Express*, *29*(18), 27961-27974. <https://doi.org/10.1364/OE.426620>
- 720 Conrad, R., Kortzak, D., Guzman, G. A., Miranda-Laferte, E., & Hidalgo, P. (2021). Ca_vbeta controls the endocytic turnover of
721 Ca_v1.2 L-type calcium channel. *Traffic*, *22*(6), 180-193. <https://doi.org/10.1111/tra.12788>
- 722 Cyganek, L., Tiburcy, M., Sekeres, K., Gerstenberg, K., Bohnenberger, H., Lenz, C., Henze, S., Stauske, M., Salinas, G.,
723 Zimmermann, W. H., Hasenfuss, G., & Guan, K. (2018). Deep phenotyping of human induced pluripotent stem cell-
724 derived atrial and ventricular cardiomyocytes. *JCI Insight*, *3*(12). <https://doi.org/10.1172/jci.insight.99941>
- 725 Del Villar, S. G., Voelker, T. L., Westhoff, M., Reddy, G. R., Spooner, H. C., Navedo, M. F., Dickson, E. J., & Dixon, R. E. (2021).
726 beta-Adrenergic control of sarcolemmal Cav1.2 abundance by small GTPase Rab proteins. *Proceedings of the*
727 *National Academy of Sciences of the United States of America*, *118*(7). <https://doi.org/10.1073/pnas.2017937118>
- 728 Di Biase, V., Tuluc, P., Campigligio, M., Obermair, G. J., Heine, M., & Flucher, B. E. (2011). Surface traffic of dendritic Cav1.2
729 calcium channels in hippocampal neurons. *Journal of Neuroscience*, *31*(38), 13682-13694.
730 <https://doi.org/10.1523/JNEUROSCI.2300-11.2011>
- 731 Dixon, R. E., Moreno, C. M., Yuan, C., Opitz-Araya, X., Binder, M. D., Navedo, M. F., & Santana, L. F. (2015). Graded
732 Ca²⁺/calmodulin-dependent coupling of voltage-gated Cav1.2 channels. *Elife*, *4*. <https://doi.org/10.7554/elife.05608>
- 733 Dixon, R. E., Navedo, M. F., Binder, M. D., & Santana, L. F. (2022). Mechanisms and physiological implications of cooperative
734 gating of clustered ion channels. *Physiological Reviews*, *102*(3), 1159-1210.
735 <https://doi.org/10.1152/physrev.00022.2021>
- 736 Emanuelli, G., Zoccarato, A., Reumiller, C. M., Papadopoulos, A., Chong, M., Rebs, S., Betteridge, K., Beretta, M., Streckfuss-
737 Bomeke, K., & Shah, A. M. (2022). A roadmap for the characterization of energy metabolism in human
738 cardiomyocytes derived from induced pluripotent stem cells. *J Mol Cell Cardiol*, *164*, 136-147.
739 <https://doi.org/10.1016/j.yjmcc.2021.12.001>
- 740 Endesfelder, U., Malkusch, S., Fricke, F., & Heilemann, M. (2014). A simple method to estimate the average localization
741 precision of a single-molecule localization microscopy experiment. *Histochemistry and Cell Biology*, *141*(6), 629-638.
742 <https://doi.org/10.1007/s00418-014-1192-3>
- 743 Ester, M., Kriegel, H.-P., Sander, J., & Xu, X. (1996). A density-based algorithm for discovering clusters in large spatial
744 databases with noise. *kdd*,
- 745 Folci, A., Steinberger, A., Lee, B., Stanika, R., Scheruebel, S., Campigligio, M., Ramprecht, C., Pelzmann, B., Hell, J. W.,
746 Obermair, G. J., Heine, M., & Di Biase, V. (2018). Molecular mimicking of C-terminal phosphorylation tunes the
747 surface dynamics of Cav1.2 calcium channels in hippocampal neurons. *Journal of Biological Chemistry*, *293*(3), 1040-
748 1053. <https://doi.org/10.1074/jbc.M117.799585>
- 749 Franzini-Armstrong, C., Protasi, F., & Ramesh, V. (1999). Shape, Size, and Distribution of Ca²⁺ Release Units and Couplons in
750 Skeletal and Cardiac Muscles. *Biophysical Journal*, *77*(3), 1528-1539. [https://doi.org/10.1016/s0006-3495\(99\)77000-](https://doi.org/10.1016/s0006-3495(99)77000-1)
751 [1](#)
- 752 Golan, Y., & Sherman, E. (2017). Resolving mixed mechanisms of protein subdiffusion at the T cell plasma membrane. *Nat*
753 *Commun*, *8*, 15851. <https://doi.org/10.1038/ncomms15851>
- 754 Grabner, M., Dirksen, R. T., & Beam, K. G. (1998). Tagging with green fluorescent protein reveals a distinct subcellular
755 distribution of L-type and non-L-type Ca²⁺ channels expressed in dysgenic myotubes. *Proceedings of the National*
756 *Academy of Sciences of the United States of America*, *95*(4), 1903-1908. <https://doi.org/10.1073/pnas.95.4.1903>
- 757 Gross, P., Johnson, J., Romero, C. M., Eaton, D. M., Poulet, C., Sanchez-Alonso, J., Lucarelli, C., Ross, J., Gibb, A. A.,
758 Garbincius, J. F., Lambert, J., Varol, E., Yang, Y., Wallner, M., Feldsott, E. A., Kubo, H., Berretta, R. M., Yu, D., Rizzo, V.,
759 . . . Houser, S. R. (2021). Interaction of the Joining Region in Junctophilin-2 With the L-Type Ca²⁺ Channel Is Pivotal for

- 760 Cardiac Dyad Assembly and Intracellular Ca²⁺ Dynamics. *Circulation Research*, 128(1), 92-114.
761 <https://doi.org/10.1161/circresaha.119.315715>
- 762 Hansen, A. S., Wroinger, M., Grimm, J. B., Lavis, L. D., Tjian, R., & Darzacq, X. (2018). Robust model-based analysis of single-
763 particle tracking experiments with Spot-On. *Elife*, 7. <https://doi.org/10.7554/eLife.33125>
- 764 Heck, J., Parutto, P., Cioraszkiewicz, A., Bikbaev, A., Freund, R., Mitlohner, J., Andres-Alonso, M., Fejtova, A., Holcman, D., &
765 Heine, M. (2019). Transient Confinement of Cav2.1 Ca²⁺-Channel Splice Variants Shapes Synaptic Short-Term
766 Plasticity. *Neuron*, 103(1), 66-79 e12. <https://doi.org/10.1016/j.neuron.2019.04.030>
- 767 Heine, M., Heck, J., Cioraszkiewicz, A., & Bikbaev, A. (2020). Dynamic compartmentalization of calcium channel signalling in
768 neurons. *Neuropharmacology*, 169, 107556. <https://doi.org/10.1016/j.neuropharm.2019.02.038>
- 769 Held, R. G., Liu, C., Ma, K., Ramsey, A. M., Tarr, T. B., De Nola, G., Wang, S. S. H., Wang, J., van den Maagdenberg, A.,
770 Schneider, T., Sun, J., Blanpied, T. A., & Kaeser, P. S. (2020). Synapse and Active Zone Assembly in the Absence of
771 Presynaptic Ca²⁺ Channels and Ca²⁺ Entry. *Neuron*, 107(4), 667-683 e669.
772 <https://doi.org/10.1016/j.neuron.2020.05.032>
- 773 Huebinger, J., Spindler, J., Holl, K. J., & Koos, B. (2018). Quantification of protein mobility and associated reshuffling of
774 cytoplasm during chemical fixation. *Sci Rep*, 8(1), 17756. <https://doi.org/10.1038/s41598-018-36112-w>
- 775 Hummert, J., Tashev, S. A., & Herten, D. P. (2021). An update on molecular counting in fluorescence microscopy. *Int J*
776 *Biochem Cell Biol*, 135, 105978. <https://doi.org/10.1016/j.biocel.2021.105978>
- 777 Jayasinghe, I., Clowsley, A. H., Lin, R., Lutz, T., Harrison, C., Green, E., Baddeley, D., Di Michele, L., & Soeller, C. (2018). True
778 Molecular Scale Visualization of Variable Clustering Properties of Ryanodine Receptors. *Cell Rep*, 22(2), 557-567.
779 <https://doi.org/10.1016/j.celrep.2017.12.045>
- 780 Jenkins, M. A., Christel, C. J., Jiao, Y., Abiria, S., Kim, K. Y., Usachev, Y. M., Obermair, G. J., Colbran, R. J., & Lee, A. (2010). Ca²⁺-
781 Dependent Facilitation of Cav1.3 Ca²⁺ Channels by Densin and Ca²⁺/Calmodulin-Dependent Protein Kinase II. *30*(15),
782 5125-5135. <https://doi.org/10.1523/jneurosci.4367-09.2010>
- 783 Kepten, E., Weron, A., Sikora, G., Burnecki, K., & Garini, Y. (2015). Guidelines for the fitting of anomalous diffusion mean
784 square displacement graphs from single particle tracking experiments. *PLoS One*, 10(2), e0117722.
785 <https://doi.org/10.1371/journal.pone.0117722>
- 786 Kleinsorge, M., & Cyganek, L. (2020). Subtype-Directed Differentiation of Human iPSCs into Atrial and Ventricular
787 Cardiomyocytes. *STAR Protoc*, 1(1), 100026. <https://doi.org/10.1016/j.xpro.2020.100026>
- 788 Koester, A. M., Szczepaniak, M., & Nan, X. (2022). Fast and Multiplexed Super Resolution Imaging of Fixed and
789 Immunostained Cells with DNA-PAINT-ERS. *Curr Protoc*, 2(11), e618. <https://doi.org/10.1002/cpz1.618>
- 790 Kuhn, T., Hettich, J., Davtyan, R., & Gebhardt, J. C. M. (2021). Single molecule tracking and analysis framework including
791 theory-predicted parameter settings. *Scientific Reports*, 11(1). <https://doi.org/10.1038/s41598-021-88802-7>
- 792 Kuzmenkina, E., Novikova, E., Jangsangthong, W., Matthes, J., & Herzig, S. (2019). Single-Channel Resolution of the
793 Interaction between C-Terminal Cav1.3 Isoforms and Calmodulin. *Biophysical Journal*, 116(5), 836-846.
794 <https://doi.org/10.1016/j.bpj.2019.01.025>
- 795 Lerner, J., Gomez-Garcia, P. A., McCarthy, R. L., Liu, Z., Lakadamyali, M., & Zaret, K. S. (2020). Two-Parameter Mobility
796 Assessments Discriminate Diverse Regulatory Factor Behaviors in Chromatin. *Molecular Cell*, 79(4), 677-688 e676.
797 <https://doi.org/10.1016/j.molcel.2020.05.036>
- 798 Lewin, L., Nsrasa, E., Golbary, E., Hadad, U., Orr, I., & Yifrach, O. (2020). Molecular and cellular correlates in K_v channel
799 clustering: entropy-based regulation of cluster ion channel density. *Sci Rep*, 10(1), 11304.
800 <https://doi.org/10.1038/s41598-020-68003-4>
- 801 Liu, G., Papa, A., Katchman, A. N., Zakharov, S. I., Roybal, D., Hennessey, J. A., Kushner, J., Yang, L., Chen, B. X., Kushnir, A.,
802 Dangas, K., Gygi, S. P., Pitt, G. S., Colecraft, H. M., Ben-Johny, M., Kalocsay, M., & Marx, S. O. (2020). Mechanism of
803 adrenergic Cav1.2 stimulation revealed by proximity proteomics. *Nature*, 577(7792), 695-700.
804 <https://doi.org/10.1038/s41586-020-1947-z>
- 805 Liu, M., Shi, G., Zhou, A., Rupert, C. E., Coulombe, K. L. K., & Dudley, S. C., Jr. (2018). Activation of the unfolded protein
806 response downregulates cardiac ion channels in human induced pluripotent stem cell-derived cardiomyocytes. *J Mol*
807 *Cell Cardiol*, 117, 62-71. <https://doi.org/10.1016/j.yjmcc.2018.02.011>
- 808 Luković, M., Geisel, T., & Eule, S. (2013). Area and perimeter covered by anomalous diffusion processes. *New Journal of*
809 *Physics*, 15(6), 063034. <https://doi.org/10.1088/1367-2630/15/6/063034>
- 810 Martens, K. J. A., Turkowyd, B., & Endesfelder, U. (2021). Raw Data to Results: A Hands-On Introduction and Overview of
811 Computational Analysis for Single-Molecule Localization Microscopy. *Front Bioinform*, 1, 817254.
812 <https://doi.org/10.3389/fbinf.2021.817254>
- 813 Michalet, X. (2010). Mean square displacement analysis of single-particle trajectories with localization error: Brownian
814 motion in an isotropic medium. *Physical Review. E: Statistical, Nonlinear, and Soft Matter Physics*, 82(4 Pt 1), 041914.
815 <https://doi.org/10.1103/PhysRevE.82.041914>
- 816 Moreno, C. M., Dixon, R. E., Tajada, S., Yuan, C., Opitz-Araya, X., Binder, M. D., & Santana, L. F. (2016). Ca²⁺ entry into
817 neurons is facilitated by cooperative gating of clustered Cav1.3 channels. *Elife*, 5. <https://doi.org/10.7554/eLife.15744>
- 818 Neef, J., Urban, N. T., Ohn, T.-L., Frank, T., Jean, P., Hell, S. W., Willig, K. I., & Moser, T. (2018). Quantitative optical
819 nanophysiology of Ca²⁺ signaling at inner hair cell active zones. *Nature Communications*, 9(1).
820 <https://doi.org/10.1038/s41467-017-02612-y>
- 821 Ovesny, M., Krizek, P., Borkovec, J., Svindrych, Z., & Hagen, G. M. (2014). ThunderSTORM: a comprehensive ImageJ plug-in
822 for PALM and STORM data analysis and super-resolution imaging. *Bioinformatics*, 30(16), 2389-2390.
823 <https://doi.org/10.1093/bioinformatics/btu202>

- 824 Papa, A., Zakharov, S. I., Katchman, A. N., Kushner, J. S., Chen, B.-X., Yang, L., Liu, G., Jimenez, A. S., Eisert, R. J., Bradshaw, G.
825 A., Dun, W., Ali, S. R., Rodrigues, A., Zhou, K., Topkara, V., Yang, M., Morrow, J. P., Tsai, E. J., Karlin, A., . . . Marx, S. O.
826 (2022). Rad regulation of Cav1.2 channels controls cardiac fight-or-flight response. *Nature Cardiovascular Research*,
827 1(11), 1022-1038. <https://doi.org/10.1038/s44161-022-00157-y>
- 828 Perni, S., & Beam, K. (2021). Neuronal junctophilins recruit specific Cav and RyR isoforms to ER-PM junctions and
829 functionally alter Cav2.1 and Cav2.2. *Elife*, 10. <https://doi.org/10.7554/eLife.64249>
- 830 Poulet, C., Sanchez-Alonso, J., Swiatlowska, P., Mouy, F., Lucarelli, C., Alvarez-Laviada, A., Gross, P., Terracciano, C., Houser, S.,
831 & Gorelik, J. (2021). Junctophilin-2 tethers T-tubules and recruits functional L-type calcium channels to lipid rafts in
832 adult cardiomyocytes. *Cardiovascular Research*, 117(1), 149-161. <https://doi.org/10.1093/cvr/cvaa033>
- 833 Pourrier, M., & Fedida, D. (2020). The Emergence of Human Induced Pluripotent Stem Cell-Derived Cardiomyocytes (hiPSC-
834 CMs) as a Platform to Model Arrhythmogenic Diseases. *Int J Mol Sci*, 21(2). <https://doi.org/10.3390/ijms21020657>
- 835 Ries, J., Kaplan, C., Platonova, E., Eghlidi, H., & Ewers, H. (2012). A simple, versatile method for GFP-based super-resolution
836 microscopy via nanobodies. *Nature Methods*, 9(6), 582-584. <https://doi.org/10.1038/nmeth.1991>
- 837 Sadegh, S., Higgins, J. L., Mannion, P. C., Tamkun, M. M., & Krapf, D. (2017). Plasma Membrane is Compartmentalized by a
838 Self-Similar Cortical Actin Meshwork. *Phys Rev X*, 7(1). <https://doi.org/10.1103/PhysRevX.7.011031>
- 839 Sahu, G., Wazen, R. M., Colarusso, P., Chen, S. R. W., Zamponi, G. W., & Turner, R. W. (2019). Junctophilin Proteins Tether a
840 Cav1-RyR2-Kca3.1 Tripartite Complex to Regulate Neuronal Excitability. *Cell Rep*, 28(9), 2427-2442 e2426.
841 <https://doi.org/10.1016/j.celrep.2019.07.075>
- 842 Sato, D., Hernandez-Hernandez, G., Matsumoto, C., Tajada, S., Moreno, C. M., Dixon, R. E., O'Dwyer, S., Navedo, M. F.,
843 Trimmer, J. S., Clancy, C. E., Binder, M. D., & Santana, L. F. (2019). A stochastic model of ion channel cluster formation
844 in the plasma membrane. *Journal of General Physiology*, 151(9), 1116-1134. <https://doi.org/10.1085/jgp.201912327>
- 845 Scharinger, A., Eckrich, S., Vandael, D. H., Schonig, K., Koschak, A., Hecker, D., Kaur, G., Lee, A., Sah, A., Bartsch, D., Benedetti,
846 B., Lieb, A., Schick, B., Singewald, N., Sinnegger-Brauns, M. J., Carbone, E., Engel, J., & Striessnig, J. (2015). Cell-type-
847 specific tuning of Cav1.3 Ca²⁺-channels by a C-terminal automodulatory domain. *Frontiers in Cellular Neuroscience*,
848 9, 309. <https://doi.org/10.3389/fncel.2015.00309>
- 849 Schindelin, J., Arganda-Carreras, I., Frise, E., Kaynig, V., Longair, M., Pietzsch, T., Preibisch, S., Rueden, C., Saalfeld, S., Schmid,
850 B., Tinevez, J. Y., White, D. J., Hartenstein, V., Eliceiri, K., Tomancak, P., & Cardona, A. (2012). Fiji: an open-source
851 platform for biological-image analysis. *Nature Methods*, 9(7), 676-682. <https://doi.org/10.1038/nmeth.2019>
- 852 Schmied, J. J., Gietl, A., Holzmeister, P., Forthmann, C., Steinhauer, C., Dammeyer, T., & Tinnefeld, P. (2012). Fluorescence and
853 super-resolution standards based on DNA origami. *Nature Methods*, 9(12), 1133-1134.
854 <https://doi.org/10.1038/nmeth.2254>
- 855 Schnitzbauer, J., Strauss, M. T., Schlichthaerle, T., Schueder, F., & Jungmann, R. (2017). Super-resolution microscopy with
856 DNA-PAINT. *Nat Protoc*, 12(6), 1198-1228. <https://doi.org/10.1038/nprot.2017.024>
- 857 Schredelseker, J., Di Biase, V., Obermair, G. J., Felder, E. T., Flucher, B. E., Franzini-Armstrong, C., & Grabner, M. (2005). The
858 beta1a subunit is essential for the assembly of dihydropyridine-receptor arrays in skeletal muscle. *Proceedings of the*
859 *National Academy of Sciences of the United States of America*, 102(47), 17219-17224.
860 <https://doi.org/10.1073/pnas.0508710102>
- 861 Schröder, T., Scheible, M. B., Steiner, F., Vogelsang, J., & Tinnefeld, P. (2019). Interchromophoric Interactions Determine the
862 Maximum Brightness Density in DNA Origami Structures. *Nano Letters*, 19(2), 1275-1281.
863 <https://doi.org/10.1021/acs.nanolett.8b04845>
- 864 Seibert, F., Rapedius, M., Fakuade, F. E., Tomsits, P., Liutkute, A., Cyganek, L., Becker, N., Majumder, R., Clauss, S., Fertig, N.,
865 & Voigt, N. (2022). A modern automated patch-clamp approach for high throughput electrophysiology recordings in
866 native cardiomyocytes. *Commun Biol*, 5(1), 969. <https://doi.org/10.1038/s42003-022-03871-2>
- 867 Siddig, S., Aufmkolk, S., Doose, S., Jobin, M.-L., Werner, C., Sauer, M., & Calebiro, D. (2020). Super-resolution imaging reveals
868 the nanoscale organization of metabotropic glutamate receptors at presynaptic active zones. *Science Advances*,
869 6(16), eaay7193. <https://doi.org/10.1126/sciadv.aay7193>
- 870 Singh, A., Gebhart, M., Fritsch, R., Sinnegger-Brauns, M. J., Poggiani, C., Hoda, J. C., Engel, J., Romanin, C., Striessnig, J., &
871 Koschak, A. (2008). Modulation of voltage- and Ca²⁺-dependent gating of Cav1.3 L-type calcium channels by
872 alternative splicing of a C-terminal regulatory domain. *Journal of Biological Chemistry*, 283(30), 20733-20744.
873 <https://doi.org/10.1074/jbc.M802254200>
- 874 Sograte-Idrissi, S., Oleksiievets, N., Isbaner, S., Eggert-Martinez, M., Enderlein, J., Tsukanov, R., & Opazo, F. (2019). Nanobody
875 Detection of Standard Fluorescent Proteins Enables Multi-Target DNA-PAINT with High Resolution and Minimal
876 Displacement Errors. *Cells*, 8(1), 48. <https://doi.org/10.3390/cells8010048>
- 877 Sograte-Idrissi, S., Schlichthaerle, T., Duque-Afonso, C. J., Alevra, M., Strauss, S., Moser, T., Jungmann, R., Rizzoli, S. O., &
878 Opazo, F. (2020). Circumvention of common labelling artefacts using secondary nanobodies. *Nanoscale*, 12(18),
879 10226-10239. <https://doi.org/10.1039/d0nr00227e>
- 880 Stanika, R., Campiglio, M., Pinggera, A., Lee, A., Striessnig, J., Flucher, B. E., & Obermair, G. J. (2016). Splice variants of the
881 Cav1.3 L-type calcium channel regulate dendritic spine morphology. *Sci Rep*, 6, 34528.
882 <https://doi.org/10.1038/srep34528>
- 883 Svendsen, S., Zimprich, C., McDougall, M. G., Klaubert, D. H., & Los, G. V. (2008). Spatial separation and bidirectional
884 trafficking of proteins using a multi-functional reporter. *BMC Cell Biology*, 9, 17. <https://doi.org/10.1186/1471-2121-9-17>
- 885 Vergnol, A., Traore, M., Pietri-Rouxel, F., & Falcone, S. (2022). New Insights in Cavbeta Subunits: Role in the Regulation of
886 Gene Expression and Cellular Homeostasis. *Front Cell Dev Biol*, 10, 880441.
887 <https://doi.org/10.3389/fcell.2022.880441>
- 888

- 889 Vierra, N. C., Kirmiz, M., van der List, D., Santana, L. F., & Trimmer, J. S. (2019). Kv2.1 mediates spatial and functional coupling
890 of L-type calcium channels and ryanodine receptors in mammalian neurons. *Elife*, 8.
891 <https://doi.org/10.7554/eLife.49953>
- 892 Vivas, O., Moreno, C. M., Santana, L. F., & Hille, B. (2017). Proximal clustering between BK and Cav1.3 channels promotes
893 functional coupling and BK channel activation at low voltage. *Elife*, 6. <https://doi.org/10.7554/elife.28029>
- 894 Weninger, G., Pochechueva, T., El Chami, D., Luo, X., Kohl, T., Brandenburg, S., Urlaub, H., Guan, K., Lenz, C., & Lehnart, S. E.
895 (2022). Calpain cleavage of Junctophilin-2 generates a spectrum of calcium-dependent cleavage products and DNA-
896 rich NT1-fragment domains in cardiomyocytes. *Sci Rep*, 12(1), 10387. <https://doi.org/10.1038/s41598-022-14320-9>
- 897 Yang, Q., Perfitt, T. L., Quay, J., Hu, L., Lawson-Qureshi, D., & Colbran, R. J. (2023). Clustering of Cav1.3 L-type calcium
898 channels by Shank3. *Journal of Neurochemistry*. <https://doi.org/10.1111/jnc.15880>
- 899 Yang, Y., Yu, Z., Geng, J., Liu, M., Liu, N., Li, P., Hong, W., Yue, S., Jiang, H., Ge, H., Qian, F., Xiong, W., Wang, P., Song, S., Li, X.,
900 Fan, Y., & Liu, X. (2022). Cytosolic peptides encoding Cav1 C-termini downregulate the calcium channel activity-
901 neuritogenesis coupling. *Communications Biology*, 5(1). <https://doi.org/10.1038/s42003-022-03438-1>
- 902 Yang, Z. F., Panwar, P., McFarlane, C. R., Tuinte, W. E., Campiglio, M., & Van Petegem, F. (2022). Structures of the
903 junctophilin/voltage-gated calcium channel interface reveal hot spot for cardiomyopathy mutations. *Proceedings of*
904 *the National Academy of Sciences of the United States of America*, 119(10), e2120416119.
905 <https://doi.org/10.1073/pnas.2120416119>
- 906 Yao, X., Gao, S., & Yan, N. (2022). Structural basis for pore blockade of human voltage-gated calcium channel Cav1.3 by
907 motion sickness drug cinnarizine. *Cell Research*, 32(10), 946-948. <https://doi.org/10.1038/s41422-022-00663-5>
- 908 Youn, Y., Lau, G. W., Lee, Y., Maity, B. K., Gouaux, E., Chung, H. J., & Selvin, P. R. (2023). Quantitative DNA-PAINT imaging of
909 AMPA receptors in live neurons. *Cell Rep Methods*, 3(2), 100408. <https://doi.org/10.1016/j.crmeth.2023.100408>
- 910 Yuan, Q., Maas, R. G. C., Brouwer, E. C. J., Pei, J., Blok, C. S., Popovic, M. A., Paauw, N. J., Bovenschen, N., Hjortnaes, J.,
911 Harakalova, M., Doevendans, P. A., Sluijter, J. P. G., van der Velden, J., & Buikema, J. W. (2022). Sarcomere
912 Disassembly and Transfection Efficiency in Proliferating Human iPSC-Derived Cardiomyocytes. *J Cardiovasc Dev Dis*,
913 9(2). <https://doi.org/10.3390/jcdd9020043>
- 914 Zaveri, S., Srivastava, U., Qu, Y. S., Chahine, M., & Boutjdir, M. (2023). Pathophysiology of Cav1.3 L-type calcium channels in
915 the heart. *Frontiers in Physiology*, 14, 1144069. <https://doi.org/10.3389/fphys.2023.1144069>
- 916 Zhang, H., Maximov, A., Fu, Y., Xu, F., Tang, T. S., Tkatch, T., Surmeier, D. J., & Bezprozvanny, I. (2005). Association of Cav1.3 L-
917 type calcium channels with Shank. *Journal of Neuroscience*, 25(5), 1037-1049.
918 <https://doi.org/10.1523/JNEUROSCI.4554-04.2005>
- 919 Zhang, Z., He, Y., Tuteja, D., Xu, D., Timofeyev, V., Zhang, Q., Glatter, K. A., Xu, Y., Shin, H. S., Low, R., & Chiamvimonvat, N.
920 (2005). Functional roles of Cav1.3 (alpha1D) calcium channels in atria: insights gained from gene-targeted null
921 mutant mice. *Circulation*, 112(13), 1936-1944. <https://doi.org/10.1161/CIRCULATIONAHA.105.540070>

Figure 1: Live-cell STED imaging resolves clustering of Halo-Ca_v1.3 at the cell surface of hiPSC-aCM.



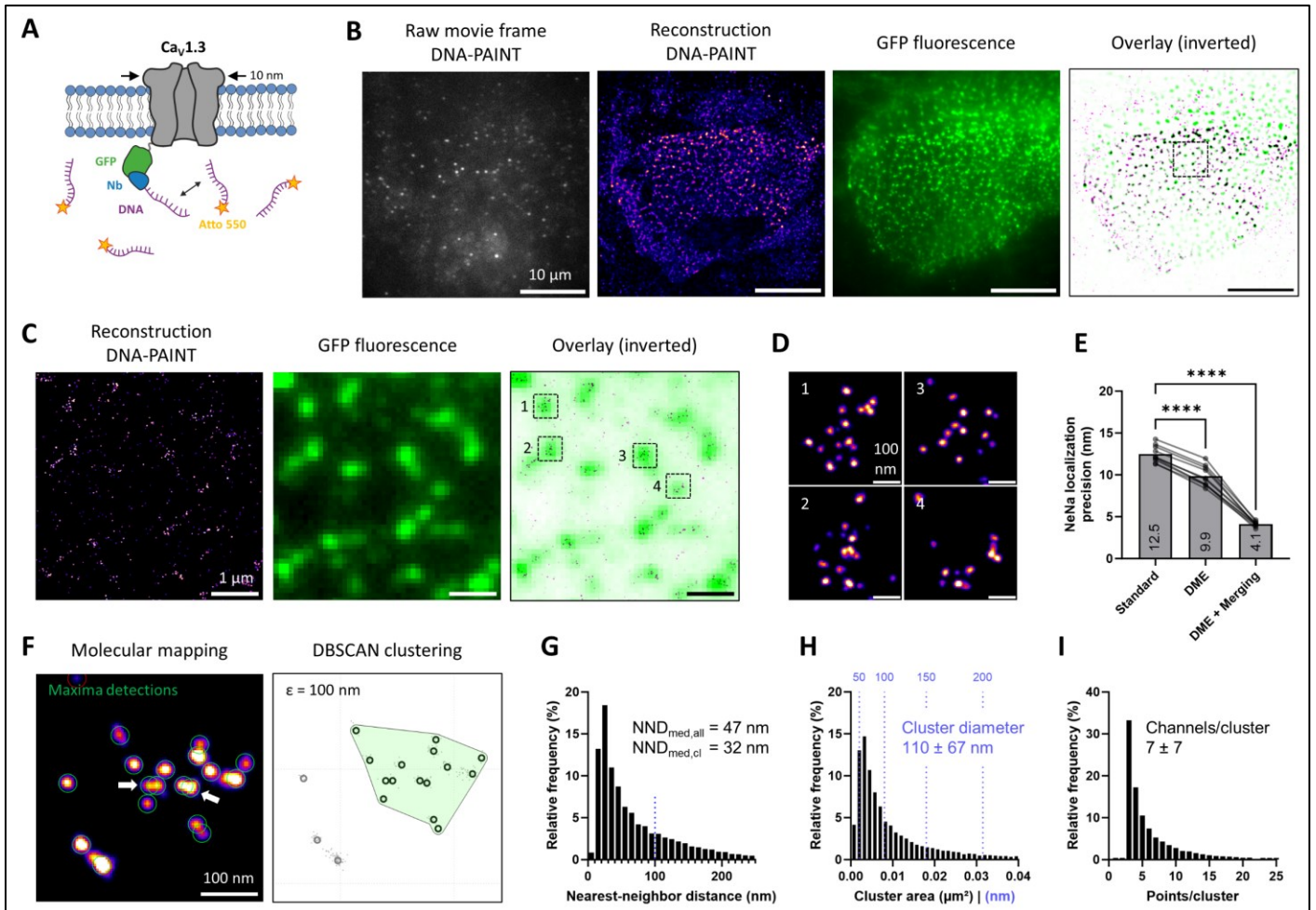
A) Halo-Ca_v1.3 fusion protein was transiently expressed in hiPSC-aCM and labeled with HTL-JF646. Live-cell confocal imaging of medial cell sections revealed predominantly spot-like signal patterns of Halo-Ca_v1.3 (magenta) distributed along the plasma membrane (green, Cholesterol-Star488), as highlighted by magnification of the indicated area.

B) Quantitative live-cell imaging was performed centering the focal plane on the basal plasma membrane (Fire' LUT). STED imaging (right column) revealed sub-diffraction size and spacing of Halo-Ca_v1.3 clusters, which could not be resolved by confocal microscopy (left). The indicated image region is magnified in the lower images, showing representative signal distributions.

C) STED images were analyzed by automated image segmentation to detect individual signal clusters at a density of $2.0 \mu\text{m}^{-2}$. Cluster sizes averaged to areas of $0.013 \pm 0.008 \mu\text{m}^2$, which were equivalent to diameters of $122 \pm 35 \text{ nm}$ assuming circular shape ($n = 10875$ clusters, $N = 30$ cells).

D) The signal mass of each cluster was referenced to calibration samples for molecular counting of labeled Halo-Ca_v1.3 inside these clusters (see Fig. S2). On average clusters contained 9 ± 12 Ca_v1.3 channels contributing to an intra-cluster channel density of $612 \mu\text{m}^{-2}$.

Figure 2: Super-resolution DNA-PAINT imaging of GFP-Cav1.3 resolves channel arrangement within clusters.



A) Illustration of DNA-PAINT labeling of GFP-tagged Cav1.3 expressed in hiPSC-aCM. After fixation, GFP was detected by docker-DNA-coupled anti-GFP nanobodies (NbGFP) and reversibly binding imager-DNA labeled by Atto643 or Atto550.

B) Single raw data TIRF imaging frames of imager dye signals were used to localize DNA-PAINT binding events, which were accumulated over 30,000–50,000 frame sequences to generate a reconstruction (Fire' LUT, blurred to enhance cluster visibility at low magnification). Simultaneous recordings of GFP fluorescence confirmed basal membrane imaging planes in transfected cells expressing GFP-Cav1.3.

C) Magnification of the indicated image region in (B), showing clusters of DNA-PAINT localization spots (left) and GFP fluorescence (center). Spatial correlation is evident in overlay images (right), confirming specificity of anti-GFP labeling with nanobodies.

D) Further magnification of exemplary clusters highlighted in (C) confirms separate, countable localization spots as a prerequisite for molecular mapping and counting of Cav1.3 channel numbers.

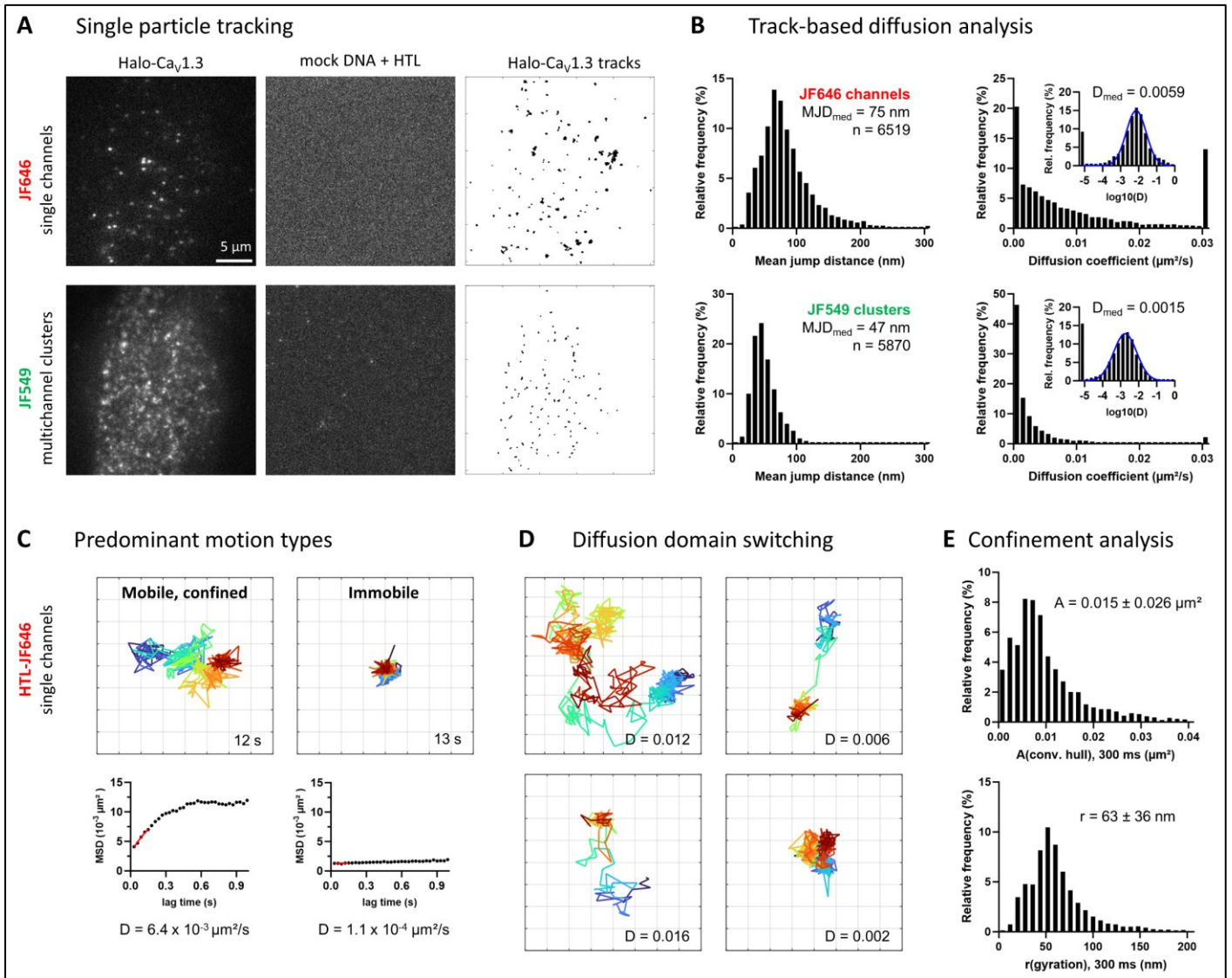
E) Drift correction (DME) and spot merging (detection time binning across 4 frames) improved the NeNA-measured localization precision from 12.5 to 4.1 nm ($N = 10$ cells). Significance was shown by repeated measures ANOVA with indicated pairwise comparisons (**** = $p < 0.0001$).

F) Molecular mapping of single channel positions was achieved by local maxima detection (indicated as green circles) from DNA-PAINT reconstructions with ≤ 5 nm localization precision (left). White arrows indicate the resolution of adjacent spots at 12 nm distance. Next, DBSCAN clustering was applied to define individual channel clusters, containing 15 channels in this example (right). DBSCAN parameters were set to $\epsilon = 100$ nm and $\text{minPts} = 3$ (see Figure S3). Molecular mapping was applied to a dataset of $n = 18129$ clusters in $N = 17$ cells.

G) Molecular maps were used to compute nearest-neighbor distances (NND) across all channel positions and restricted to DBSCAN-defined clusters. The blue-dotted line indicates a plateau of NND values at 100 nm in line with the optimal ϵ parameter.

H) Molecular maps and DBSCAN cluster outlines were used to determine the distribution of cluster area and channel counts (I) in reconstructed DNA-PAINT data. Additional median and interquartile range (IQR) values are shown in Table 1.

Figure 3: Single channel tracking quantifies the mobility and confinement of clustered $\text{Ca}_v1.3$ channels.



A) Single-molecule TIRF images of a living hiPSC-aCM expressing Halo- $\text{Ca}_v1.3$ channels (first column) and a corresponding mock-transfected control cell (second column). Cells were concurrently labeled for individual channels (250 pM HTL-JF646, first row) and multichannel clusters (50 nM HTL-JF549, second row). For each recorded cell, an image series of multichannel clusters (JF549) was recorded, followed by a second image series of single channels (HTL-JF646). The image data of both labeling modes was independently processed by single-particle-tracking (SPT). The resulting tracks are shown as an overlay for the exemplary cell (third column).

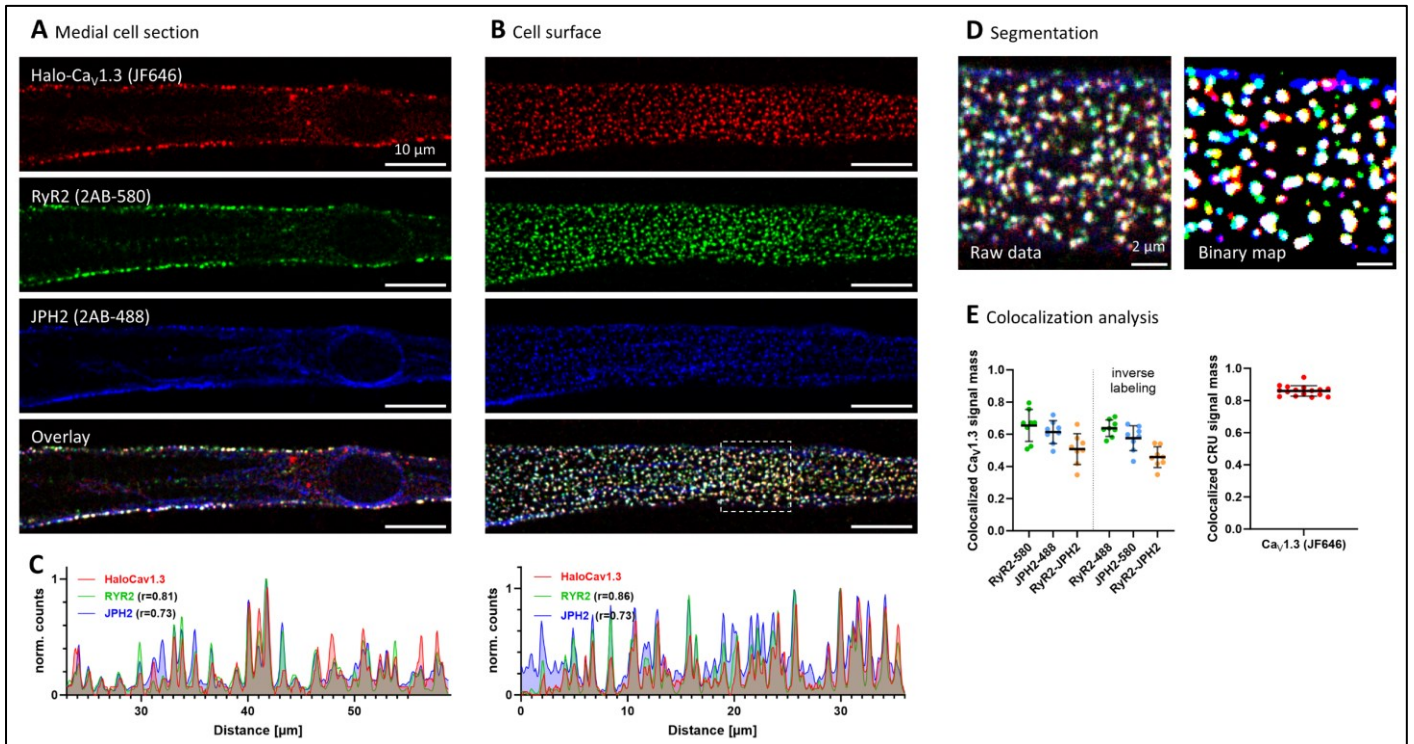
B) The diffusion of individual channels and clusters is compared by histograms depicting the mean jump distance of tracks and the diffusion coefficient originating from a fit of time-dependent mean-squared-displacement (MSD) curves. Insets show the same data on a logarithmic scale with gaussian fit curves in blue and median values indicated above. D value histograms include under- and overflow bins for values outside of the axis range. The dataset includes $N = 15$ cells with $n = 6519$ single channel tracks and $n = 5873$ cluster tracks.

C) Exemplary tracks of JF646-labeled single channels with duration > 10 s demonstrate the two predominant motion types: Mobile, confined (left) and immobile (right). The corresponding MSD curves are shown on the right side, with a red line indicating the linear fit used to retrieve the diffusion coefficient. The grid interval is 100 nm.

D) Exemplary single-channel tracks show occasional domain and motion type switching, characterized by intermittently high mobility traversal between multiple domains of lower mobility and high confinement.

E) Confinement analysis was performed on sufficiently long tracks containing at least 10 localizations. Two metrics were used to characterize local confinement: The convex hull area surrounding each complete track, and the radius of gyration. Both metrics were computed over a 300 ms (10 frame) sliding time window to avoid the inclusion of multi-domain track segments.

Figure 4: Colocalization of Cav1.3 with JPH2 and RyR2 in surface-localized calcium release units.



A) Live-cell labeling of Halo-Cav1.3 expressed in hiPSC-aCM was combined with subsequent RyR2 and JPH2 immunofluorescence for confocal imaging. Medial confocal sections display Cav1.3 (red), RyR2 (green) and JPH2 (blue) only in the cell periphery, where they show extensive colocalization (white coloring), representing calcium release units (CRU) localized to the plasma membrane. '2AB-' indicates the secondary antibody conjugate and corresponding imaging channel (580 = Abberior Star580, 488 = Abberior StarGreen).

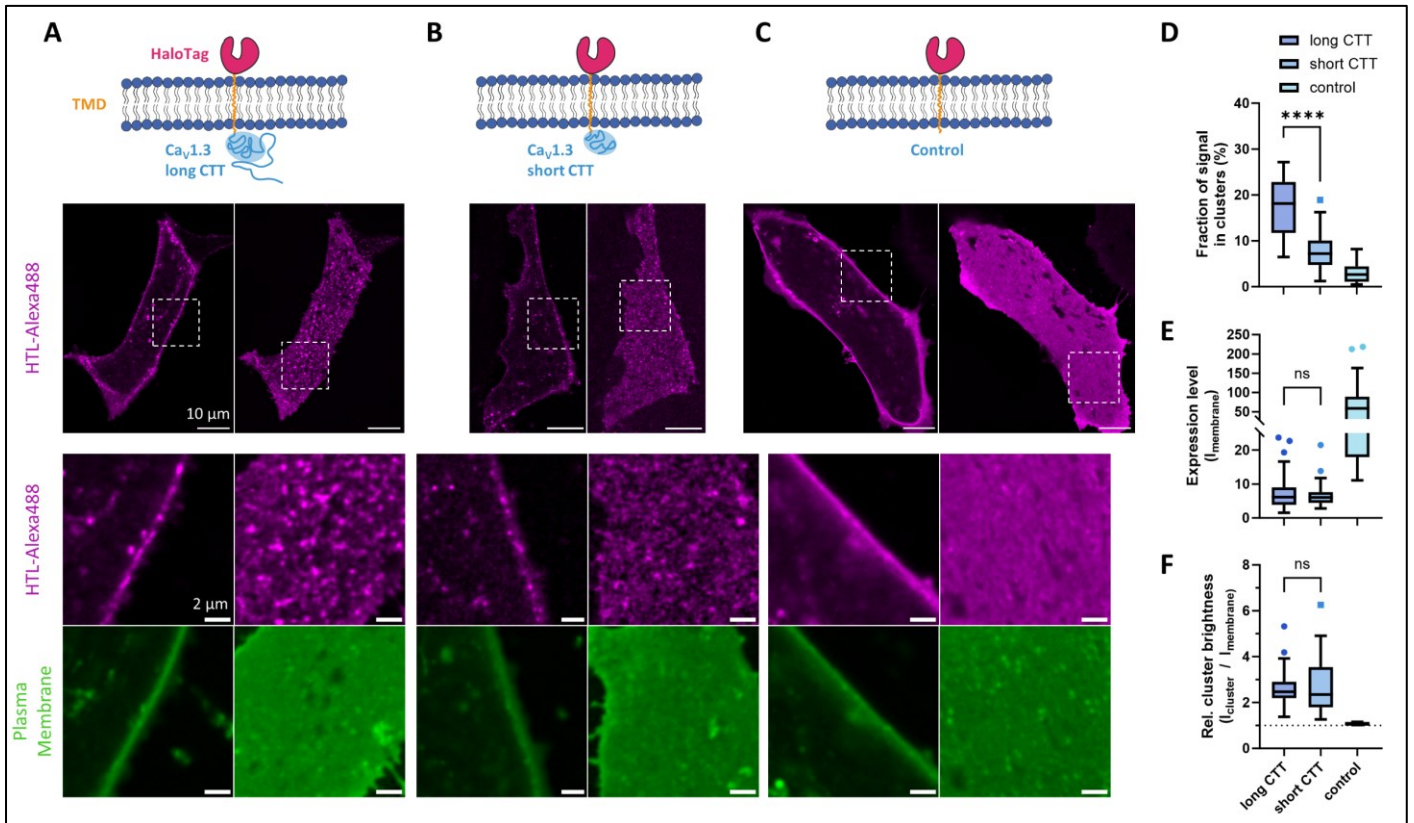
B) Imaging of the adherent, basal plasma membrane in the same cell reveals a homogeneous 2D distribution of spot-like signals, representing adjacent, plasma membrane resident CRUs.

C) Representative line profiles across cluster signals demonstrate extensive spatial correlation between fluorescent signals corresponding to all three analyzed CRU proteins. The Pearson correlation coefficient (r) indicates one-dimensional correlation of each RyR2 and JPH2 to Halo-Cav1.3 signal.

D) Three channel images from planar membranes (magnification from B) were segmented for signal-spots and binarized. Consequently, white signal color indicates three-channel colocalization, magenta indicates Cav1.3-JPH2, yellow indicates Cav1.3-RyR2 and cyan indicates RyR2-JPH2 colocalization, respectively.

E) Colocalization analysis quantified the fraction of Cav1.3 signal mass overlapping with binarized areas of either RyR2, JPH2 or both (left graph). Specific colocalization was confirmed with an inversion of fluorophores on secondary antibodies. The right graph shows the fraction of CRU signal mass (defined by the product of RyR2 and JPH2 signal) that is colocalized with Cav1.3-binarized area ($N = 16$ cells).

Figure 5: Cav1.3 C-terminal construct expression in hiPSC-aCM leads to cluster formation.



A) A fusion protein of Cav1.3₄₂ C-terminal tail (long CTT) attached to transmembrane-HaloTag was expressed in hiPSC-aCM using transient transfection. After live-cell labeling with cell-impermeable HTL-Alexa488, distinct spot-like signals resembling Cav1.3-like clusters were revealed at the cell surface by confocal imaging in the medial (left) and basal (right) imaging plane (displayed in magenta). The localization was confirmed by co-staining with the plasma membrane marker Cellmask-DeepRed (displayed in green).

B) Expression of the equivalent fusion protein containing the short CTT of Cav1.3 splice variant 42A also lead to cluster-like signal shapes at the cell surface. However, cluster-like spots appeared less abundant compared to the long isoform shown in **(A)**.

C) A control construct containing only transmembrane-HaloTag showed a homogenous protein distribution in the plasma membrane without the formation of distinct, cluster-like spots.

D) Evaluation of confocal HTL-Alexa488 signal distributions shown in **(A-C)** by cluster analysis. Cluster signals were detected by automatic thresholding after gaussian filtering of images and then quantified by size and brightness. Box plots show Median, IQR and Tukey-based whiskers. The fraction of clustered signal within basal plasma membranes was significantly larger for long vs short CTT (**** = $p < 0.0001$, Welch's unpaired t-test, N = 28, 29, 25 cells). The control condition showed an absence of significant clustering and was therefore not statistically compared.

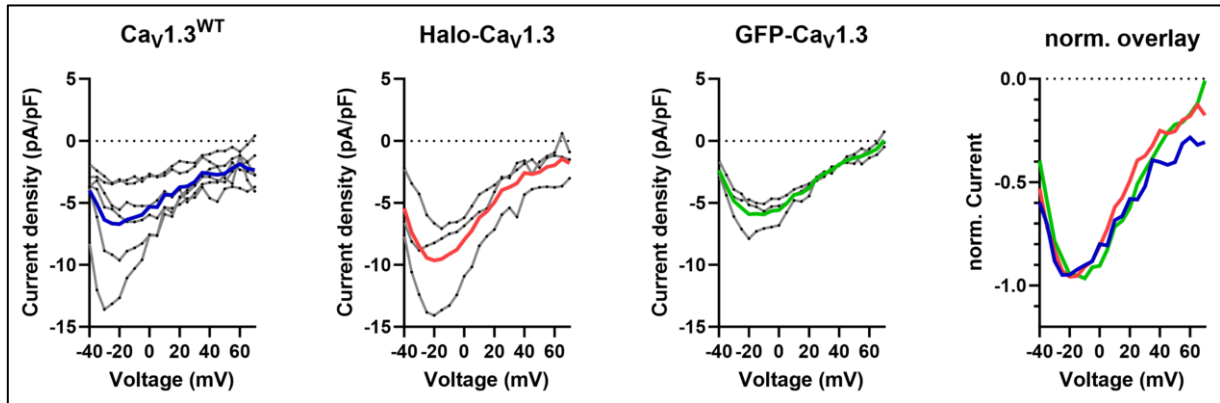
E) Membrane expression levels measured by the average fluorescence intensity showed no significant difference between long and short CTT ($p = 0.47$).

F) Similarly, the relative signal intensity of clusters compared to the whole plasma membrane showed no significant difference between long and short CTT ($p = 0.7$).

Table 1: Comparison of cluster analysis results generated by STED imaging and DNA-PAINT

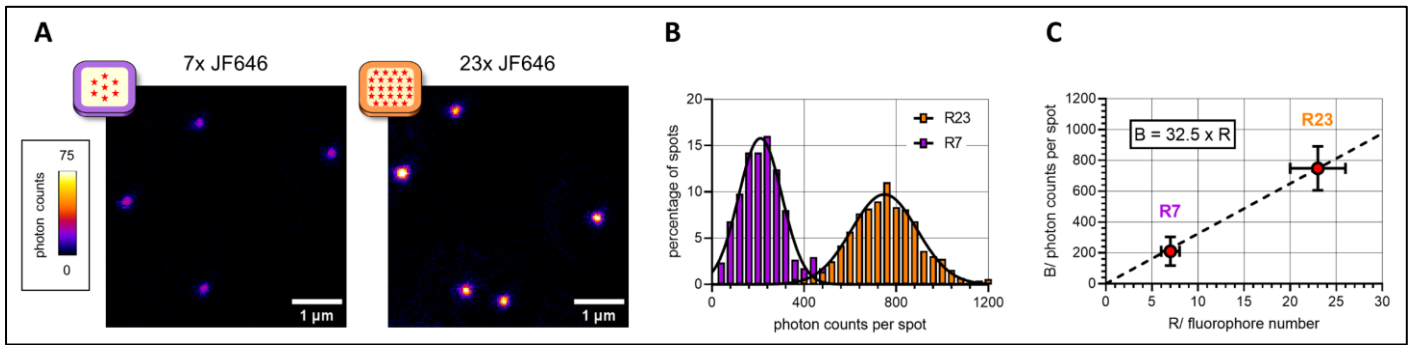
Cluster measurements	Mean \pm SD, STED	Mean \pm SD, DNA-PAINT	Median, STED	Median, DNA-PAINT	IQR STED	IQR DNA-PAINT
Cluster area (μm^2)	0.013 \pm 0.008	0.013 \pm 0.020	0.011	0.006	0.008 – 0.016	0.003 – 0.014
equivalent diameter (nm)	122 \pm 35	110 \pm 67	116	89	98 – 141	64 – 135
Channel count per cluster	8.8 \pm 12	6.9 \pm 6.6	5	4	3.1 – 10.7	3 – 8
Intra-cluster channel density (μm^{-2})	612 \pm 510	898 \pm 580	527	726	391 – 749	501 – 1101
Summary statistics	Mean \pm SD, STED	Mean \pm SD, DNA-PAINT	N cells, STED	N cells, DNA-PAINT	n clusters, STED	n clusters, DNA-PAINT
Cluster density (μm^{-2})	2.0 \pm 0.5	2.5 \pm 0.5	30	17	10875	18129
Clustered channel fraction (%)	-	61 \pm 5				

Figure S1: Automated patch clamp measurements of wild-type and tagged $\text{Ca}_v1.3$ channels expressed in HEK293 cells confirm similar electrophysiological characteristics.



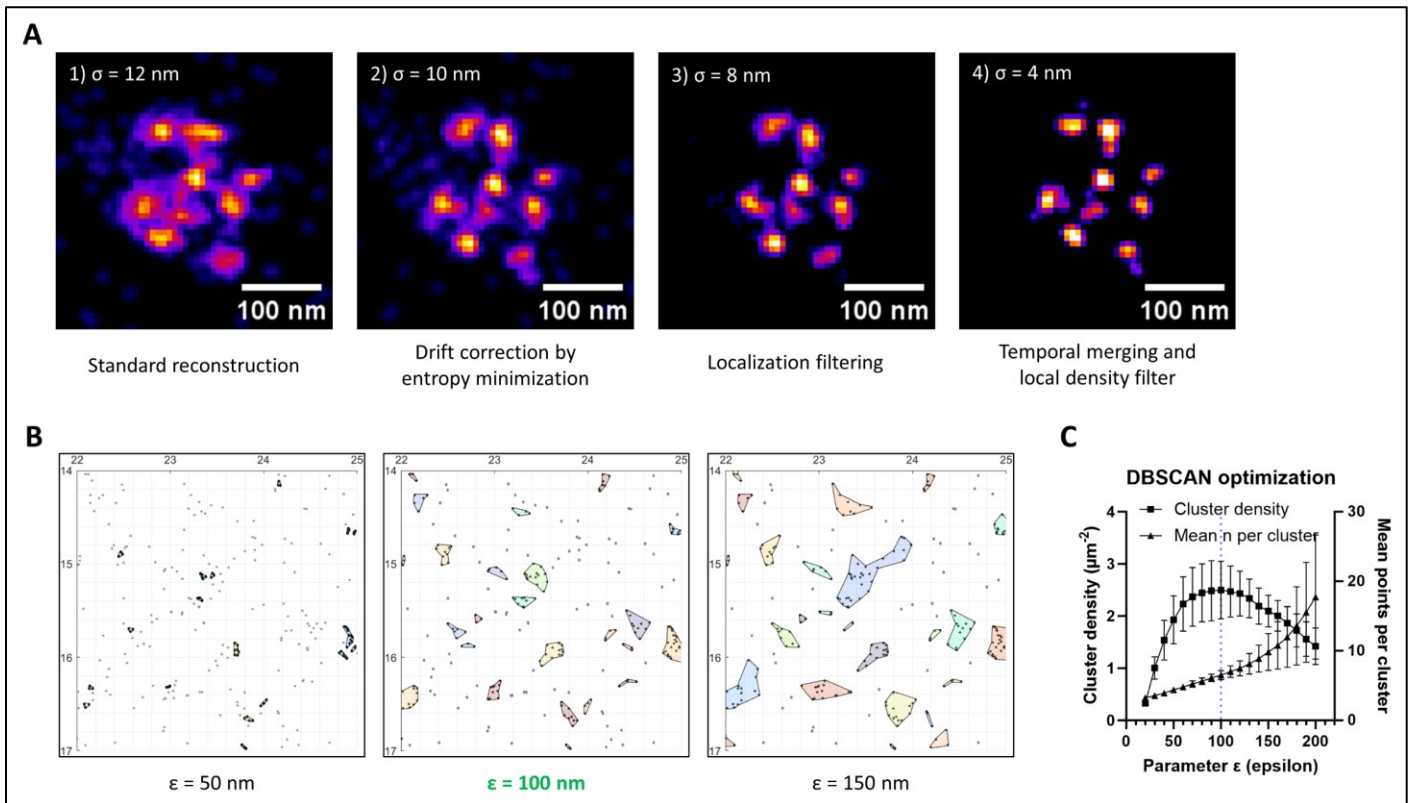
HEK293 CT6232 cells expressing accessory β_3 and $\alpha_2\delta_1$ subunits were induced to express $\text{Ca}_v1.3^{\text{WT}}$ or transfected with plasmid encoding Halo- or GFP-tagged $\text{Ca}_v1.3$ channels. Whole-cell calcium currents were measured using the Nanion SyncroPatch 384 device. The resulting IV curves of individual cells are shown as gray lines and averaged for each condition (colored lines). The last graph shows an overlay of the averaged IV curves for each condition after normalizing current amplitude minima to -1 a.u. to account for the variation in channel expression levels.

Figure S2: Brightness referencing method for molecular counting of JF646 fluorophores.



DNA Origami linked to 7 or 23 JF646 dye molecules were immobilized on coverslips and recorded by STED imaging under equal conditions as for cellular Halo-Cav1.3 cluster imaging (A). By image analysis of spot-like signals, a distribution of integrated photon counts across all detected spots was determined for each sample (B). The histograms were fitted by normal distributions to retrieve mean brightness values, which was used for a linear fit of spot brightness to dye molecule counts in (C). The determined conversion factor (32.5 photon counts per fluorophore) was used for image analysis of Halo-Cav1.3 samples to retrieve labeled channel counts within clusters.

Figure S3: Optimization of DNA-PAINT image reconstruction and DBSCAN clustering.

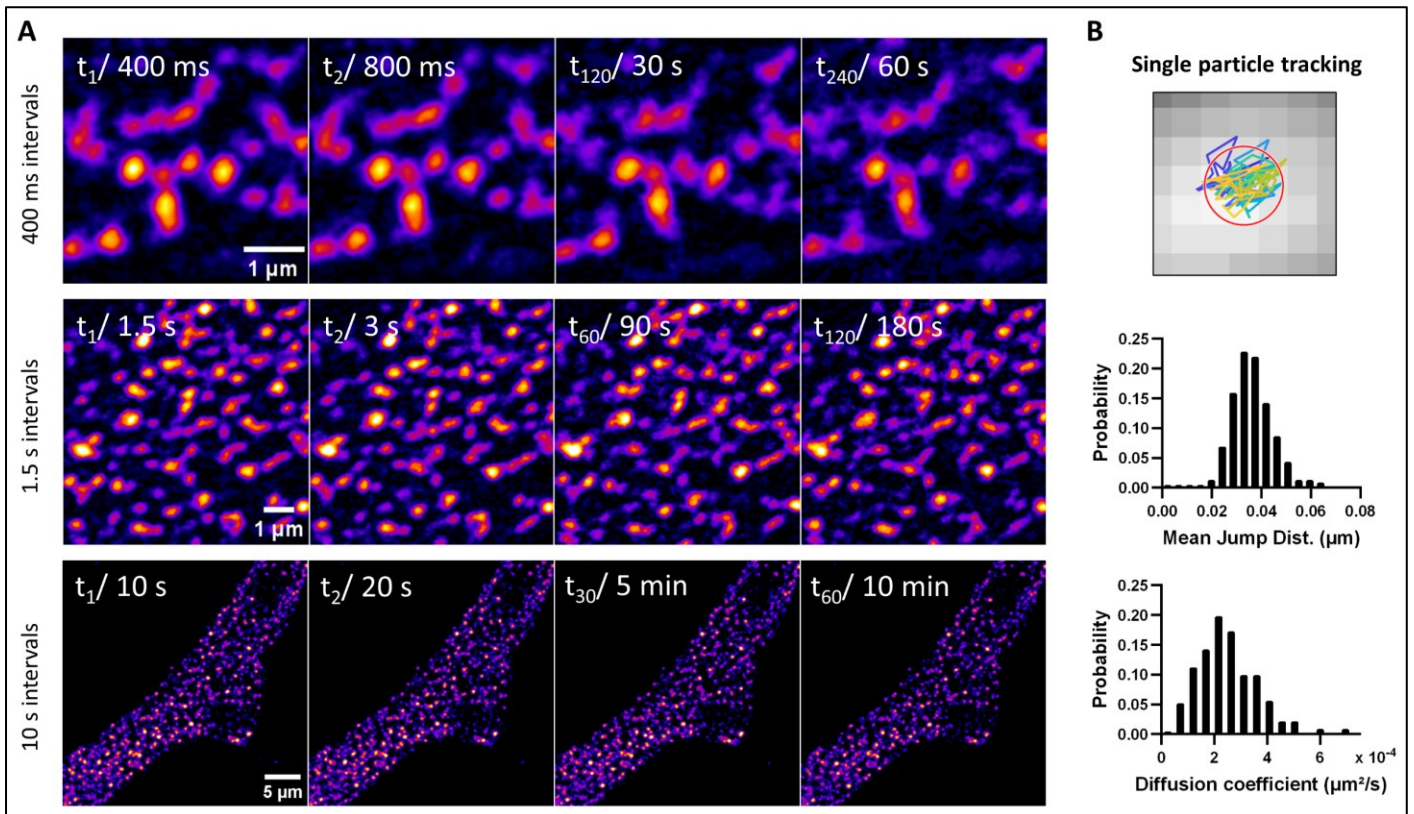


A) Representative reconstruction of a GFP-Cav1.3 channel cluster imaged by DNA-PAINT in TIRF mode. A successive improvement of the localization-based image reconstruction over standard reconstruction (1) was achieved by applying a customized version of drift correction by entropy minimization (DME, 2), followed by either histogram-based localization filtering (3), or followed by temporal merging of subsequent localizations and local density filtering (4).

B) The point clustering algorithm DBSCAN was applied to DNA-PAINT molecular map data. Three exemplary values for the parameter ϵ give rise to distinct clustering results.

C) Graph showing the change in DBSCAN cluster density and points per cluster as a function of ϵ parameter values at $\text{minPts} = 3$. For $\epsilon = 100$ nm, the highest cluster density ($2.5 \mu\text{m}^{-2}$) is observed, while higher ϵ values lead to merging of pre-existing clusters and increased heterogeneity.

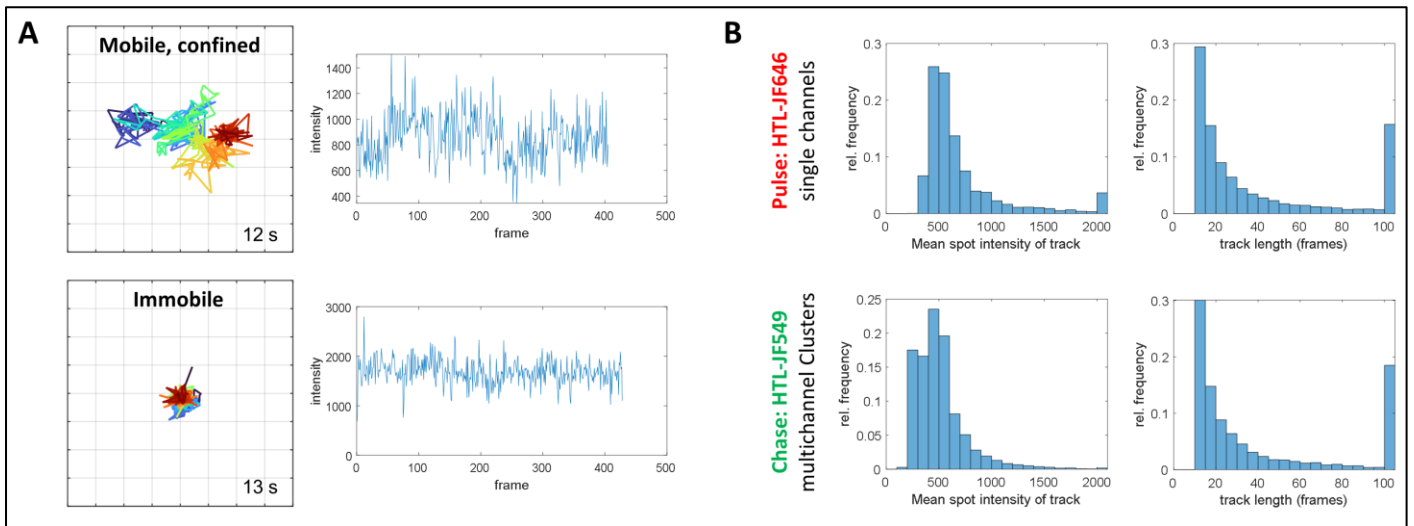
Figure S4: Confocal timelapse imaging demonstrates immobility of Halo-Cav1.3 clusters across time scales.



A) Confocal timelapse imaging of hiPSC-aCM expressing Halo-Cav1.3 (row 1+2) or GFP-Cav1.3 (row 3) shows cluster positions in the basal plasma membrane. Images series were recorded in intervals of 400 ms, 1.5 s and 10 s. For each timelapse, the first, second, middle and last frame are shown.

B) Representative trajectory of a single cluster position shown on a 30 nm pixel grid, generated by SPT of a timelapse at 1.5 s intervals and 30 nm pixel size. Quantitative analysis of SPT data reveals low jump distances of $\sim 35\text{ nm}$ reflecting the localization uncertainty and MSD fit-derived diffusion coefficients of less than $10^{-4}\text{ }\mu\text{m}^2/\text{s}$, thus confirming immobility of the tracked cluster positions.

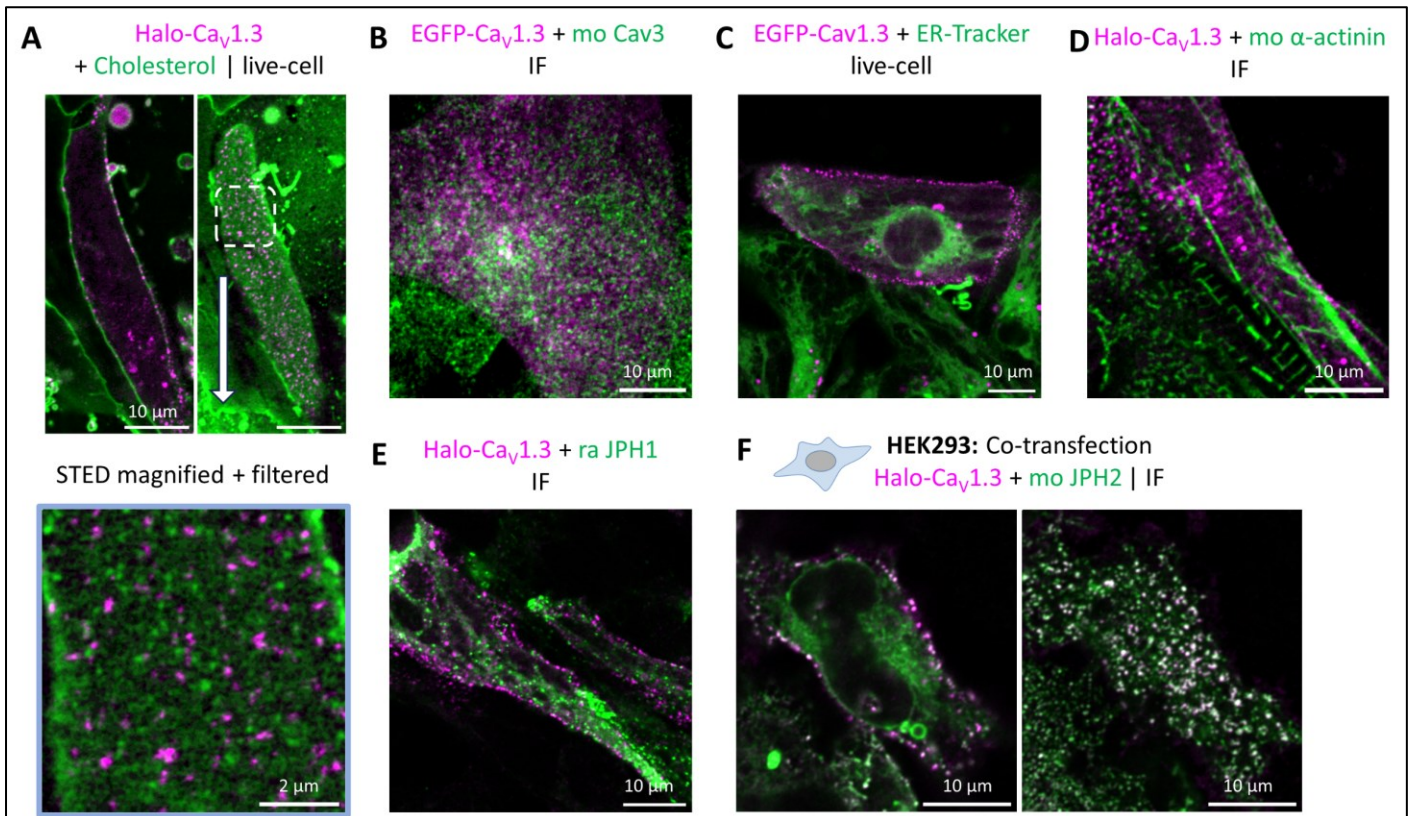
Figure S5: Supporting data for single particle tracking analysis.



A) Intensity time traces for the exemplary tracked spots shown in Figure 3C. No bleaching steps were observed in the majority of long tracks.

B) Mean spot intensity and track length distributions indicative of tracking performance were calculated. Both metrics show similar distributions for both imaging modes, which excludes a potential bias in the comparative diffusion analysis.

Figure S6: Halo-Cav1.3 colocalization with nanodomain and compartment markers.



A) Live-cell confocal images of hiPSC-aCM expressing Halo-Cav1.3, labeled by HTL-JF646 and Cholesterol-StarOrange. Cav1.3 clusters and Cholesterol both localized to the plasma membrane (top), but dual-channel STED imaging in the basal membrane focal plane (bottom) showed rather exclusion-like arrangement with Cholesterol-containing nanodomains.

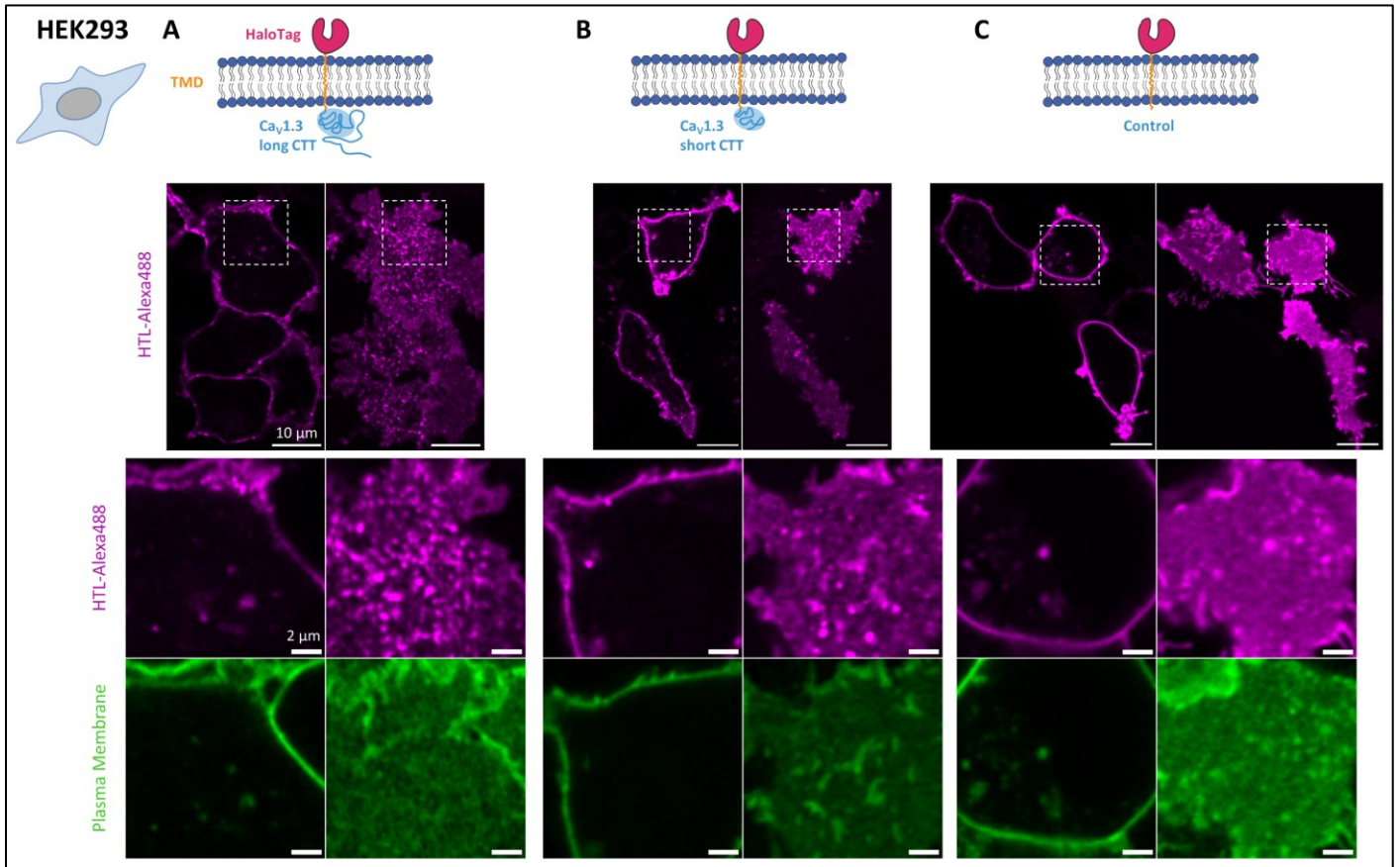
B) Immunofluorescence of hiPSC-aCM expressing EGFP-Cav1.3 showed rather low colocalization with Caveolin-3 (Cav3).

C) Live-cell imaging of hiPSC-aCM showed a mutually exclusive distribution of EGFP-Cav1.3 and endoplasmic reticulum, labeled by ER-Tracker Red.

D) Immunofluorescence of hiPSC-aCM expressing Halo-Cav1.3 showed no colocalization with cardiac α -actinin or Junctional Protein-1 (JPH1) (**E**).

F) Immunofluorescence of HEK293 CT6232 cells transfected with Halo-Cav1.3 and JPH2-CFP showed extensive colocalization of clustered spots in the basal membrane focal plane.

Figure S7: Ca_v1.3 C-terminal construct expression in HEK293 leads to cluster formation independent of the cardiac proteome.



A) Ca_v1.3 C-terminal cytosolic tail (CTT, long isoform) fused to cell-surface HaloTag was expressed in HEK293 CT6232 cells and labeled with cell-impermeable HTL-Alexa488. The cells were co-stained with the plasma membrane marker Cholesterol-PEG-KK114 and imaged by live-cell confocal microscopy.

B) Expression of the equivalent fusion protein containing the short C-terminal tail splice variant.

C) Expression of a control construct containing only cell-surface HaloTag without CTT sequence, serving as a negative control.

Figure S8: Illustration of the custom-built optical setup (described in the Methods section)

